https://doi.org/10.5194/egusphere-2023-1692
Preprint. Discussion started: 28 July 2023

Anatomy of a fumarole field; drone remote sensing and petrological approaches reveal the degassing and alteration structure at La Fossa cone, Vulcano Island, Italy

Daniel Müller[1], Thomas R. Walter[1], Valentin R. Troll[2,3], Jessica Stammeier[1], Andreas Karlsson[3], Erica de Paolo[4], Antonino Fabio Pisciotta[5], Martin Zimmer[1], Benjamin De Jarnatt[1]

[1] GFZ German Research Centre for Geosciences, Telegrafenberg, 14473 Potsdam, Germany
[2] Dept. of Earth Sciences, Natural Resources and Sustainable Development, Uppsala University, Sweden
[3] Department of Geosciences, Swedish Museum of Natural History, Box 50007, SE-104 05 Stockholm, Sweden
[4] University of Milano-Bicocca, Department of Earth and Environmental Sciences, Piazza della Sciencza 4 – 20126 Milano, Italy
[5] Istituto Nazionale di Geofisica e Vulcanologia (INGV), Palermo, Italy

Correspondence to: Daniel Müller (dmueller@gfz-potsdam.de)

https://doi.org/10.5194/egusphere-2023-1692
Preprint. Discussion started: 28 July 2023

Abstract. Hydrothermal alteration processes can affect the physical and chemical properties of volcanic rocks and develop via complex degassing and fluid flow systems and regimes. Although alteration can have far-reaching consequences for rock stability and permeability, little is known about the detailed structures, extent, and dynamic changes that take place in hydrothermal venting systems. By combining drone-based remote sensing with mineralogical and chemical analyses of rock and gas samples, we analyzed the structure and internal anatomy of a dynamic evolving volcanic degassing and alteration system at the La Fossa cone, Vulcano Island (Italy). From drone image analysis, we revealed a ~70,000 m² sized area subject to hydrothermal activity, for which we could determine distinct alteration gradients. By mineralogical and geochemical sampling of the zones of those alteration gradients, we study the relation between surface coloration and mineralogical and chemical composition. With increasing pixel brightness towards higher alteration gradients, we find a loss of initial mineral fraction and bulk chemical composition and a simultaneous gain in sulfur content. Using this approach, we defined and spatially constrained alteration units and compared them to the present-day thermally active surface and degassing pattern. The combined results permit us to present a detailed anatomy of the La Fossa fumarole field, highlighting 7 major units of alteration and present-day diffuse activity that, next to the high-temperature fumaroles, significantly contribute to the total activity.

1 Introduction

1.1 Volcanic degassing and hydrothermal alteration

Volcanic degassing at the Earth's surface is typically expressed in the form of localized fumarole fields and diffuse gas escape, yet the association of localized and diffuse degassing is not well constrained. A fumarole is a vent or opening in the Earth's surface that releases steam and gas, including sulfur dioxide, carbon dioxide, and hydrogen sulfide, into the atmosphere (e.g. Giggenbach, 1996, Giammanco et al., 1998, Halldorsson et al., 2013). Fumaroles are typically found near volcanic areas or geothermal regions where there is intense heat beneath the surface. Fumaroles are of interest to scientists studying volcanoes and geothermal systems, as they provide information on the composition of underlying magmatic systems, the degassing processes of such magmatic systems, and the dynamic changes in the degassing passways exploited by such systems (e.g. Chiodini et al., 1993, Aiuppa et al., 2005, Paonita et al., 2013). The gas emissions by fumaroles, moreover, provide information on the possible interaction between underground water and hot rocks or magma and thus the state of a hydrothermal system through time (e.g. Chiodini et al., 1993, Capasso et al., 2000, Nuccio et al., 2001, Troll et al., 2012, Paonita et al., 2013).

The degassing of hot and acid volcanic gasses leads to versatile fluid-rock interactions at the surrounding volcanic rock, summarized as hydrothermal alteration (Pirajno, 2009, Chiodini et al., 2013, Fulignati, 2020). Alteration can affect the mineral assemblage by dissolution and remineralization up to complete destruction of the original mineral matrix and eventually influence essential rock parameters with potentially far-reaching consequences for the shallow hydrothermal system and the stability of a volcanic building (Reid & Brien, 2001, Heap & Violay, 2021). Mechanical strength tests of

https://doi.org/10.5194/egusphere-2023-1692
Preprint. Discussion started: 28 July 2023

hydrothermally altered rocks showed considerable mechanical weakening (e.g. Heap et al., 2019, Julia et al., 2014, Darmawan et al., 2022), which is usually accomplished by mineral dissolution and mineral re-precipitation that affect rock strength and permeability and can in cases even seal gas pathways. Hydrothermal alteration can thus lead to sealed rock masses and hence to pressure build-up in a shallow volcanic system and consequently influence volcanic activity (e.g. Heap et al., 2019). It is therefore important to better understand the degassing and alteration structures in active hydrothermal crater regions of hazardous volcanic systems.

In this study of the fumaroles of La Fossa Vulcano Island - Italy, we aim to detect and quantify alteration-related spatial and compositional parameters in order to provide improved insight into the dynamic changes of hydrothermal venting systems to help identify temporal and potentially critical developments and to better understand the associated features of diffuse and localized degassing.

1.2 Structure and extent of degassing sites

Recent advances in volcanic geothermal areas suggest that fumaroles are often only localized expressions of a much larger area of degassing (e.g Toutain et al., 2009, Liuzzo et al., 2015). Indeed, fumaroles and hydrothermal degassing zones are often accompanied by broader fields of activity, characterized by diffuse degassing processes, associated mineral changes, and intense surface recoloration (e.g. Donoghue et al., 2008, Berg et al., 2018, Darmawan et al., 2022) and fumaroles activity can vary in time (Troll et al., 2012, Fischer et al., 2015) and in size (Lynch et al., 2013, Gertisser et al 2023). Previous works at Vulcano, for instance, have shown that fumaroles are surrounded by extensive areas of diffuse degassing (Carapezza et al., 2011, Chiodini et al., 2005, Manini et al., 2019). Our previous work showed that diffuse degassing leads to distinct zones classified by temperatures and visual expression (Müller et al., 2021). Those diffuse zones are also constrained based on CO_2 measurements but are also subject to the diffuse flow of acid gas driving diffuse alteration processes. However, these diffuse degassing and alteration processes are often difficult to recognize without specialized sampling strategies (Toutain et al., 2009), leading to a limited understanding of the anatomy and extent of degassing and alteration systems. Understanding the dynamic changes and internal architecture of hydrothermal activity of fumarole fields and the true dimensions of their field of activity is of relevance for the study of volcanic hazards and resources.

1.3 Surface effects and remote sensing of alteration

Hydrothermal alteration can cause significant changes in the physical and chemical properties of volcanic rock, such as density, compressive strength, and permeability (e.g. Donoghue et al., 2008, 2010, Berg et al., 2018, Heap et al., 2019, Darmawan et al., 2022). The replacement of primary minerals by secondary minerals, element mobility of fluid-mobile components, enrichment of refractory elements, and physical and textural changes of rock properties are often accompanied by changes in the color or spectral reflectance characteristics and can be traced employing remote sensing techniques.

https://doi.org/10.5194/egusphere-2023-1692
Preprint. Discussion started: 28 July 2023

Several studies have investigated the relationship between coloration and hydrothermal alteration. The use of rock color or spectral reflectance particularities as an indicator of alteration has been explored since the 1970s and led to the development of a variety of remote sensing techniques using satellite imagery from ETRS multispectral imagery (Rowan et. al., 1976), Landsat Thematic mapper mission (Carranza et al., 2002), ETM+ (Mia et al., 2012) or ASTER data (Di Tommaso et al., 2007) or hyperspectral analysis (e.g. Van De Meer et al., 2012, Tayebi et al., 2015). These techniques can detect subtle changes in color that may not be visible to the naked eye, allowing for the identification of mineral deposits (Mielke et al., 2016), hydrothermal alteration, or volcano stability (Kereszturi et al., 2020).

However, for analyzing details of localized degassing and alteration systems, the resolution of satellite data often is a limiting factor. Some of the best available optical satellite data have a resolution of 0.5 m in the nadir acquisition position. The resolution of thermal satellite data is on the order of tens to hundreds of meters per pixel. That allows the general detection of degassing and alteration systems, but the imaging of details of such systems requires the use of very high-resolution data. Modern UAS (unmanned aerial systems) equipped with high-resolution sensors allow imaging of volcanic surfaces at cm scales and, therefore, permit the analysis of degassing and alteration systems in great detail. In combination with Structure from Motion (SfM) processing, they are efficient for first-site investigations and allow the creation of high-resolution structural maps to identify structures of degassing systems to assist first-order hazard analysis or guide further in-depth studies.

1.4 Aim of the study

The aim of this work is to image and analyze the degassing and alteration structure of the La Fossa fumarole field and better understand the association of diffuse and localized degassing at a fumarole field. We advance previous results (Müller et al., 2021) by considering new data, and by integrating them with the mineralogical and chemical analysis of alteration distribution in collected rock samples. We show systematic changes in the effects of alteration on the surface coloration and how drone-derived RGB data (Red, Green, Blue, standard color coding of images) can be used for the efficient detection and classification of degassing and alteration features. Combining UAS-based optical and infrared remote sensing with mineralogical- and geochemical analysis, and diffuse surface degassing measurements, we can infer the detailed anatomy of degassing and alteration systems at the surface, highlight active degassing domains versus areas of surface sealing, and determine their importance for the system based on their contribution to the total thermal energy release.

2 Study area

Vulcano is the southernmost of a group of 7 small volcanic islands forming the Aeolian Archipelago north of Sicily. They are located within the Aeolian Tindary Letojanni Fault System (ATLFS), an NNW-SSE striking local deformation belt connecting the central Aeolian Islands with the eastern section of Sicily (Barreca et al., 2014, Cultrera et al., 2017). The ATLFS is the interface between two larger tectonically active compartments, an extensive one in the northeast and a

https://doi.org/10.5194/egusphere-2023-1692
Preprint. Discussion started: 28 July 2023

contractional one in the west (Cultrea et al., 2017). Frequent seismic activity and right lateral extensional displacements indicate ongoing tectonic activity (Billi et al., 2006) and the active shaping of the islands.

Vulcano is made up of volcanic edifices of which the northern section of the islands is the most recently active. The oldest volcanic activity at Vulcano is reported for 130 ka (De Astis et al., 2013). 6 main stages of volcanic activity have been identified (De Astis et al.1997), of which the geologically younger active parts, the La Fossa Cone and Vulcanello, have been active during historical times <8 ka, showing mainly vulcanian and strombolian activity (De Astis et al., 2013). The last eruptive period of the La Fossa Cone from 1888-1890 was characterized by strong phreatic eruptions and witnessed and documented by Guiseppe Mercalli who later coined the term Vulcanian eruptions (Clarke et al., 2015).

Vulcano since then is in a quiescent period and volcanic activity mainly expresses in degassing. Gases are provided from a magmatic-hydrothermal system fed by a shallow magmatic reservoir beneath La Fossa volcano. The hydrothermal system is likely to have been partitioned into a hypersaline brine and a vapor phase (Henley and McNabb, 1978). The denser brine phase is confined at depth and contributes to the formation of metasomatic facies observed in deep-seated xenoliths (Adrian et al., 2007). The vapor phase, enriched with SO_2, H_2S, HCl, and HF, ascends to the surface and partly emerges directly from the high-temperature fumarolic field (Bolognesi and D'Amore, 1993; Chiodini et al., 2000; Capasso et al., 1997).

Volcanic degassing is present throughout the entire central and northern part of the island concentrating in degassing clusters at Baja Di Levante, within Vulcano Porto, and in clusters along the base and summit of La Fossa Cone (Chiodini et al., 1996, Carapezza et al., 2011, Diliberto et al., 2021, Inguaggiato et al., 2022 and many others) where frequently higher fluxes of CO_2 are observed. The most prominent degassing sites are the high-temperature fumaroles at the summit of Vulcano that occur in several clusters on the outer rims of La Fossa cone and are most prominent in the high-temperature fumarole field (Figure 1). Degassing at the summit of La Fossa is persistent but subject to fluctuations. Gases of the high-temperature fumaroles (HTF) emerge with temperatures >300 °C, but temperatures have been exceeded in the past. Temperatures of >500 °C were reported (Harris et al., 2012, Diliberto, 2017) during previous volcanic crises.

Several periods of unrest have been reported and were accompanied by increasing fumarole temperatures (Harris et al., 2012, Diliberto, 2013, Madonia et al., 2013, Diliberto, 2017), increasing soil and groundwater temperatures (Capasso et al., 2014), changing gas compositions (Paonita et al., 2013), changes in gas flux (Inguaggiat et al., 2022), or a spatial growth of the fumarole field (Bukomirovic et al., 1997). The most recent crisis occurred in 2021 and led to increased thermal radiation (Coppola et al., 2022), deformation (INGV Bulletin reports), and localized structural changes like the formation of new major fumarole complexes. The rapid dynamics during volcanic crises and potentially negative effects of alteration on permeabilities, and therewith the potential to drain gases from the surface, highlight the importance of a better understanding of the structure and state of degassing systems.

Early studies about the structural setup of the Grand Cratere fumarole field of the La Fossa Cone were provided by Bukumirovic et al. (1997) and later modified (Madonia et al., 2016, Harris et al., 2009). Fulignati et al. (1999) analyzed alteration facies at Vulcano and constrained the central crater region to be a large silicic alteration complex characterized by

https://doi.org/10.5194/egusphere-2023-1692
Preprint. Discussion started: 28 July 2023

the presence of chalcedony and amorphous silica. Outwardly to the central silicic alteration zone, advanced argillic (alunite ± gypsum) alteration develops, probably originating from the progressive neutralization of the acid fluids by weathering and dilution by meteoric waters (Fulignati et al., 1998). Müller et al. (2021) previously showed that degassing and alteration can be traced from remote sensing data far beyond the extent of the high-temperature fumarole locations. Based on surface color variability due to degassing and alteration processes they showed evidence for a more complex setup with alteration gradients within the silicic alteration complex and important structural units that will be complemented here. Examples for degassing and alteration-related surface color variability are shown in Figure 2.

3 Data and methods

To analyze the degassing and alteration structure at Vulcano, we used a combination of UAS-derived remote sensing data (optical and thermal infrared imagery), image analysis, and field-based ground-truthing by mineralogical and geochemical analysis of rock samples and surface degassing measurements. A simplified sketch of the workflow is shown in Figure 3.

1) An anomaly detection (chapter 3.2) based on UAS-derived data, employing image analysis techniques like Principal Component Analysis (PCA), and spectral and thermal classification (similar to Müller et al., 2021) provides the detailed optical and thermal anomaly pattern. Anomalies can be revealed based on slight color changes in the volcanic surface that occur due to degassing and hydrothermal alteration processes, or increased surface temperatures.

2) To verify observed anomalies, we carried out ground-truthing by mineralogical (XRD X-Ray Diffraction) and geochemical (XRF X-Ray Fluorescence) lab analyses of representative rock samples. Further, we performed surface degassing measurements to image the present-day degassing pattern and compared it to the observed anomaly pattern. Combining this information we can infer a detailed anatomy of the degassing and alteration structure at the surface and define and parameterize major structural units.

3) A temporal Infrared-monitoring carried out from 2018 to 2022, covering the volcanic crisis 2021 at Vulcano allows us to monitor the thermal evolution and response of the identified units to an event of increased gas flow with further implications of critical processes like localized surface sealing.

Details on the single analysis steps are provided below.

3.1. Acquisition and processing of UAS-based optical and thermal infrared data

The data acquisition was performed using a DJI Phantom 4 Pro quadcopter, equipped with a gimbal-stabilized 20 MP camera with a real shutter system, recording up to 0.5 HZ. Optical overflights were performed in the daytime at an altitude of 150 m above the fumarole field, ensuring a minimum overlap of 90 % for later photogrammetric processing. Thermal infrared image data was acquired by a Flir Tau 2 radiometric thermal infrared camera system attached to the DJI Phantom 4

https://doi.org/10.5194/egusphere-2023-1692
Preprint. Discussion started: 28 July 2023

Pro. The FLIR Tau 2 measures in the spectral range of thermal infrared between 7.5 and 13 µm, has a resolution of 640 x 512 pixels and is a fully radiometric sensor system. The infrared image data is recorded at 8 Hz by a Teax Thermal Capture 2 data logger. The camera was attached to the copter with a standard camera bracket on a self-made carrier frame and is powered by an external 11.1 V lithium-polymer battery, supplying voltage to the camera system (transformed down to 5.2 V in) and to an external GPS antenna (>8V required) which provides coordinates for each infrared image. Infrared overflights were performed in the early morning hours, before the sun illuminates the crater area, to avoid disturbances of irregular surface heating due to solar radiation exposure (Stevenson and Varley, 2008). In this way, we ensure to map the thermal signal from the hydrothermal system exclusively.

All image data were processed using the Structure from Motion (SfM) approach in Agisoft Photoscan (Version 1.5.2.7838). The image data were inspected and images were preselected ensuring an overlap of 90%. Images of poor quality or out of focus were excluded and only images of a constant flight altitude were used for the processing. This is particularly important for the processing of infrared data, as varying altitudes might alter the radiation information due to changing pixel size to vent ratios. The infrared data was pre-inspected in Thermoviewer 3.0 and exported in a 16-bit tiff format in grayscale. We followed the typical workflow of sparse point cloud-, dense point cloud- and mesh generation, aiming to obtain a 3-dimensional model and eventually orthomosaic, digital elevation model (DEM), and infrared mosaic. The original images and processing results are roughly georeferenced, but their geolocation was optimized by manual co-registration using the ArcGIS georeferencing toolbox. An overview of the acquired and processed data sets can be found in Table 1.

3.2 Anomaly detection - Principal Component Analysis (PCA) and spectral classification for alteration mapping

The alteration mapping was performed on an orthomosaic data set acquired in 2019 that, due a poor fumarole activity, provides an almost distortion-free image of the central crater region. Using an approach similar to Müller et al., (2021), the alteration structure was revealed by applying a Principal Component Analysis allowing further constraints on the zonation of the fumarole area and expanding the interpretation by geochemical and mineralogical ground truthing. PCA is a statistical tool that can detect and highlight optical anomalies within an RGB data set by transforming the data values of the initial RGB channels onto their perpendicular axes of the highest data variance. The resulting Principal Components are variance representations and can be used to detect and highlight optical anomalies like color changes due to alteration processes. PCA further promotes a decorrelation of the initial RGB bands, a dimensionality reduction, and associated better data separability so that color variations, before expressed by changes in the three RGB bands (3-dimensional problem), can now be accessed in single bands, the single Principal Components (PC). While Principal Component 1 (PC) resembles ~91.3 % (95) of the initial data variance, it mainly shows brightness changes within the image. PC 2 and 3 contain 7.4 (4.5) and 2.3 (0.5) % of the data variance, resemble color changes, and are suitable to resolve optical anomalies related to hydrothermal alteration.

https://doi.org/10.5194/egusphere-2023-1692
Preprint. Discussion started: 28 July 2023

Hydrothermally altered areas were defined based on the PC3, with pixel values > 85 representing hydrothermal alteration. We used this as a mask to crop the respective pixel locations in the original orthomosaic, resulting in a 16 Mio pixel alteration raster subset. This raster subset allows for a more sensitive image analysis due to the reduced spectral range with respect to the original orthomosaic. An unsupervised classification (implemented in ArcGIS) with 32 classes was applied to the PCA of the hydrothermal alteration raster subset and used to classify optical units. By combining classes in a way that they resemble optical spatial units best, we defined 4 Types of surface (Types 1-4) and analyzed their spectral characteristics and spatial distribution. Boxplots of the distribution of RGB values in the 32 classes and the spectral range of Type 1-4 surfaces are shown in Appendix A. The optical structure of the fumarole field and alteration zone is similar to the thermal structure and will be discussed in Chapter 4.3.

3.3 Infrared analysis - thermal structure and time series analysis

The SfM-derived infrared mosaic represents the thermal radiation in a 16-bit tiff format, resembling values between 0 and 65536. To obtain a temperature map from the IR mosaic we calculated the apparent pixel temperatures Tp by

$$Tp\ (\text{in K}) = \text{grayvalue} * 0.04 \quad (1)$$

where Tp is the apparent pixel Temperature in K, gray value is the radiation value of the original infrared mosaic and 0.04 is the scaling factor (radiometric resolution). The thermal structure was analyzed by defining temperature thresholds above background temperature, that highlight thermal spatial units best. A temperature threshold of T>40°C was used to highlight high-temperature fumarole (HTF in the following) locations and a threshold of >22°C-40°C (min. 5 °C above background) highlights areas of a rather diffuse thermal surface heating (Figure 4 B/D). To compare the thermal emissions of detected structural units, we calculate radiant flux and radiant exitance values by applying the modified Boltzmann law.

$$Q = e*b*A*(Tp4-To4) \quad (2)$$

The emissivity (e) was assumed to be 0.95 (often used as an assumption for volcanic surfaces), the Boltzmann constant (b) is 5.670737x10-8 Wm-2K4, the area of a pixel (A) is 0.024 m². *Tp* is the pixel temperature and *To* is the average background mean temperature, calculated based on 9 reference areas that are anomaly free. The flight altitude of 150 m (above the fumarole field) in combination with the low resolution of infrared sensors results in a pixel resolution of 0.38x0.38 m.

Note that remotely sensed Infrared data always represents apparent temperatures that might differ from the real object temperature due to the radiation properties of the measured object itself (emissivity), the distance of the sensor to the measured object, the pixel-to-object size ratio, but also due to atmospheric or hydro-meteorological effects (Ball and Pinkerton, 2006) influencing the detected radiation values. Therefore apparent temperatures typically are lower than in situ

https://doi.org/10.5194/egusphere-2023-1692
Preprint. Discussion started: 28 July 2023

vent temperatures. Real fumarole vent temperatures can reach more than 300 °C (Diliberto, 2013) while temperatures in our infrared mosaic range to max. 163 °C only. With this data set, we do not aim to provide precise fumarole temperatures but to analyze the thermal structure of the fumarole field and the broader field of activity.

3.4 Ground-truthing by Mineralogical and geochemical analysis

3.4.1 Rock sampling

Rock samples were collected at predefined representative locations aiming to include all alteration end members, during field campaigns in 2019 and 2022. We sampled along 3 transects following the postulated hydrothermal alteration gradients and crosscutting major alteration units, of which transect A is located on the lower fumarole field, transect b along the upper crater rim, and transect c is located in the eastern crater crosscutting several alteration units (locations for samples in chapter 4.2.2). Samples were in the size of ~2000cm³ (hand-sized) retaining the undisturbed surface crust, but also subsurface material to a depth of ~ 10 cm. The samples were mechanically crushed, ground to 63 µm, and split for XRD and XRF analysis, respectively. In total 21 samples were collected of which 9 were prepared for the XRD and XRF analysis and 12 for XRF analysis exclusively.

3.4.2 X-ray diffraction (XRD)

Between 1 and 3 mg of whole rock powder was used to determine the mineral composition of each sample through powder X-ray diffraction (pXRD). The analysis was conducted using a PANalytical X'pert diffractometer equipped with an X'Celerator silicon-strip detector at the Department of Geoscience, Swedish Museum of Natural History, Stockholm. The instrument was operated at 45 kV and 40 mA using Cu-Kα radiation (λ = 1.5406 Å). Samples were analyzed between 5° and 70° (2θ) for 20 min in step sizes of 0.017° in continuous scanning mode while rotating the sample. Data were collected with "divergent slit mode" and converted to "fixed slit mode" for Rietveld refinement. The collected data show several peaks of X-ray diffraction intensity which represent the characteristic of crystalline minerals, the proportions of mineral phases were then refined using the Rietveld refinement method in the High Score Plus 4.6e software. The XRD analytical procedure was performed twice for each sample to ensure optimal quality control. Some samples contained contents of amorphous material of more than 50%. Those will be marked with a * in the following but we will consider the mineral composition normalized to 100 % non-amorphous material.

https://doi.org/10.5194/egusphere-2023-1692
Preprint. Discussion started: 28 July 2023

3.4.3 X-ray fluorescence (XRF)

Bulk chemical composition was determined by X-ray fluorescence analysis (XRF) at the ElMiE Lab at the German Center for Geosciences (GFZ). Main and trace elements were measured on fused beads with an AXIOS spectrometer (Malvern Panalytical, UK). Loss of ignition (LOI) was determined by analysis of H_2O/CO_2 using an Eltra element analyzer. Reproducibility was determined on three certified reference materials (CRM) and is within the analytical precision, which is better than 2% for main elements and better than 10% for trace elements.

3.4.4 Surface degassing measurements (CO_2, SO_2, H_2S)

The surface degassing was measured at ~ 200 points within the northern part of the La Fossa cone (Figure 6) in September 2021 and November 2022 using a simplified multi-gas accumulation chamber approach (Appendix B). The measurement unit, a Dräger XAM 8000 handheld Multigas device, was equipped with 6 sensors measuring CO_2, CH_4, SO_2, H_2S, H_2, and O2 simultaneously of which CO_2, SO_2, and H_2S are considered here. The simplified accumulation chamber approach was an adaption as a consequence of uncertainties encountered in previous multi-gas measurement campaigns. Due to different sensor reaction times for ascending and especially descending gas concentrations, the comparison of direct sensor readings might lead to odd gas ratios with an artificial shift towards magmatic components. For that reason, we use the slope of the ascending gas concentration within a defined volume as quantification for a relative surface flow. More detailed information about the gas measurement approach is provided in the supplementary materials. Note that the aim of the gas measurements was not to provide accurate flux estimates but to highlight the spatial variability of the gas flow of certain gas species from the surface.

4 Results

4.1 Thermal- and optical anomaly pattern reveal degassing and hydrothermal alteration structures

Degassing and hydrothermal alteration at La Fossa as seen in drone imagery can be traced by mainly two effects.
1) The transition from unaltered to hydrothermally altered surface can be traced by a general color shift in the drone images from reddish to grayish (Figure 2A and 4A). This allowed us to constrain a distinct ~770,000 m² sized area surrounding the fumarole field in a circumferential manner. This area is hereafter referred to as the Alteration Zone (ALTZ in Figure 4A/B), and represents the maximum extent of at surface observable alteration effects that can be associated with the fumarole field. It includes effects ranging from weak surface alteration to strong alteration with intense surface bleaching and remineralization, to complete destruction of the host material. The extent of the ALTZ exceeds the area covered by the high-temperature fumarole (HTF) site by ~50 times (Figure 4A/B), indicating the widespread influence of diffuse degassing and alteration processes.

https://doi.org/10.5194/egusphere-2023-1692
Preprint. Discussion started: 28 July 2023

2) Within the ALTZ we observe a segmentation characterized by brightness and color variability expressed in different shades of gray (Figure 4A), the second optical effect, indicating local alteration gradients. Analyzing the ALTZ for this spectral variability by PCA and image classification we can constrain pixels of low-, increased-, or intense surface bleaching and alteration (light blue, dark blue, and red pixels in Figure 4B) and define an alteration index represented by 4 surface Types (1-4), of which Type 1 is the most altered and Type 4 the least altered surface.

Type 1 surfaces are bright grayish intensely bleached surfaces or sulfuric deposits and represent the strongest alteration end members that we can detect optically from our data. Type 1 mainly resembles the fumarole sites and surrounding areas (Figure 4 A/B) but also larger isolated regions that can not be associated with major vent systems. With increasing distance to the degassing centers, we observe a shift towards darker grey (Type 2) and brownish (Type 3) surface colors. **Type 2** is characterized by a gray but comparatively less bright coloring. It typically occurs at the boundaries between Type 1 and Type 3 regions and largely surrounds Type 1 areas, but it also forms several isolated clusters typically embedded in Type 3 areas (units b,d,g in Figure 4). Type 3 is generally darker and more reddish in color, similar to the unaltered parts of the crater surface, but can be well distinguished from the unaltered surfaces by PCA. It makes up ~50% of the ALTZ and dominates in the central northern and the south-eastern parts. Type 4 is a reddish, apparently oxidized surface that dominates the La Fossa cone surrounding the ALTZ.

The surfaces within the ALTZ are generally mixed and composed of more than one type. The ALTZ is characterized by a generally high density of Type 3 pixels, with locally high densities of Type 1 and Type 2 pixels, which then become the dominant surface Type and form larger spatial units, indicating locally higher alteration gradients or larger structural units (units a-g in Figure 4 and details in Appendix C). The largest of these units cover several thousand square meters.

The thermally active surface (Figure 4C) can be divided into high-temperature fumaroles (HTF in Figure 4D) and diffuse thermally active surface (green pixels in Figure 4D). HTFs are the visible part of the activity that can be constrained by the naked eye in the field, while the diffuse thermally active surface is largely imperceptible. The thermally active surface largely mirrors the alteration pattern observed in the optical data. An analysis of the temperatures obtained at all pixels of Type 1 to 4 surface show a general increase of mean pixel temperatures from Type 4 to Type 1 surface by an average of 2 degrees (Figure 5). In particular, areas dominated by Type 1 and 2 surfaces reflect the thermal structure well while areas of Type 3 dominance largely coincide with low-temperature surfaces (Figure 4 B/D). An additional Spearman correlation test, applied to the classified surface (32 classes unsupervised, for comparison see Appendix A) and the thermal data (in °C) shows a moderate positive correlation between optical and thermal anomalies (Appendix D). This shows that the detected optical anomalies are meaningful and that degassing and alteration variability occurs even at local scales and can be traced in our close-range drone remote sensing data.

The spatial coincidence of both optical and thermal anomalies highlights the relationship between variations in the surface coloration, caused by alteration processes, and the ongoing influence of diffuse gas flow. A general coincidence of

https://doi.org/10.5194/egusphere-2023-1692
Preprint. Discussion started: 28 July 2023

increasing brightness (simultaneously increasing the RGB values) with increasing surface temperature of an area can be constrained (Figure 5).

4.2 Anomaly structure revealed from optical and thermal data

The optical and thermal anomalies form distinct spatial units of alteration and elevated surface temperature (units a-g in Figure 4D), which now allow us to infer the following surface structure of the fumarole field and its wider field of activity.

The centers of degassing activity are high-temperature fumaroles (HTF). These are the "visible" part of the activity that can be perceived in the field (red pixels in Figure 4D). We spatially constrain the HTFs based on apparent temperature values with T>40°C in our 150 m overflight data. Using this as a threshold we find that the HTFs cover an area of 1223 m², and occur exclusively in the Type 1 surface. However, HTFs represent only a fraction of the active surface.

The total extent of the surface that has to be considered active is much larger. The surface with elevated temperature covers ~30000 m² (green pixels in Figure 4D, T>22°C or 5°C above the background), exceeding the area covered by HTF by a factor of 25. The surface that is considered hydrothermally altered (ALTZ ~70,000 m²) exceeds the area covered by HTF by a factor of ~60, highlighting the widespread influence of diffuse degassing and alteration processes.

Besides the HTF we have constrained larger units of elevated surface bleaching and surface temperatures that can be considered structurally important and centers of diffuse degassing activity.

Units a and b are diffuse features of increased surface bleaching (Type 1 and 2) and surface temperature, embedded in the Type 3 surface and surrounding the eastern fumarole field in the form of an aureole shape. Neither can be associated with major vents. The observed maximum surface temperature for unit a is 43.7°C (0.43 m resolution) and the average temperature is 25°C, ~8 °C above the background. It is located at a distance of 25 to 50 m downslope from the eastern rim fumarole complexes, separated by a low-temperature zone (LTZ). Unit b, the southern part of the aureole is a 120 m long and 20 - 35 m wide anomaly located subparallel on the inner side of the crater. It extends over ~2100 m² and has a maximum surface temperature of 46°C and an average temperature of 26°C (9° C above the background). The temperature range and spatial extent of units a and b are comparable. In the field, both are difficult to identify as there is little or no evidence of degassing (Appendix E). Like unit a, unit b is also separated from the main fumarole vents by the LTZ. Its northern boundary corresponds exactly to the positions and curvature of the fumarole alignments at a relatively constant distance of 30 meters. In unit b, we observe a temperature gradient with higher temperatures at greater distances from the fumarole vents and an apparently more active center in the south-eastern corner. Another thermal anomaly with a similar shape and orientation is located further south inside the crater.

Units d and f are similar aureole-like features in the western fumarole field, associated with fumarole complex F0. They circumferentially surround fumarole complex F0 at a distance of 5 to 15 m, also separated from the HTF by a Low-Temperature Zone (LTZ), but to a lesser extent than that observed for units a and b of the eastern fumarole field. The southwestern section of this aureole, unit d, appears as a larger heated complex with stronger surface bleaching (Type 1) and higher temperature (mean T=27°C), and a temperature gradient with higher temperatures further away from the major fumarole complex. The boundary to the low-temperature zone is sharp with a sudden drop in temperature of 10 to 20 °C and

https://doi.org/10.5194/egusphere-2023-1692
Preprint. Discussion started: 28 July 2023

strong associated color shift (Appendix C). The aureoles of F0 and F11 have in common that they are encircled by a network of polygonal net-shaped thermal anomalies in the far field.

Low-temperature zones (LTZs) dominate the central parts of the fumarole field. The LTZ have only slightly elevated temperatures relative to the background (18-21°C or 1-4°C above background) and can be optically constrained by a darker Type 3 surface coloration. From field observations, we have constrained that these LTZ form a strong, apparently sealed surface complex. Therefore LTZ might indicate largely sealed sections of the fumarole field which inhibit gas flow at the surface. The 3 central LTZ1-3 (Figure 4D) cover an area of ~12,000 m².

Unit c is a broad complex of highly altered material (Type 1) and significantly high surface temperatures. It is potentially the most altered member in the central crater region. It covers an area of ~8000 m² and the maximum and average apparent temperatures observed are 87 °C and 29 °C. It is associated with the HTF FA and F58. Considering the thermal structure of unit e, it is a heterogeneous unit formed by a network of higher temperature anomalies embedded in lower but, with respect to the background, significantly increased tempered surface. This area is associated with the northwestern crater unit, which is the most recent explosion crater.

Unit e is a large branching thermal and optical anomaly of the upper fumarole field. It can be constrained by its gray coloration embedded in the reddish unaltered surface and also by its increased surface temperature. It is a 120 to 150-m-long branch-shaped network of anomalies on the inner crater wall. The central feature is oriented E-W and located ~ 20 m south and below the helicopter platform and the crater rim. We constrained its size to ~2500 m² (only the western branch, without intersection to h) and the recorded maximum and average apparent temperatures are 45.0 °C and 25.9 °C respectively. Some smaller clusters of localized degassing, alteration, and increased surface temperature are observed in the northern section of the fumarole field (unit g) towards La Forgia.

4.2 Ground truthing - verification of observed anomalies

We have carried out mineralogical (X-ray diffraction) and geochemical (X-ray fluorescence) analyses of bulk rock samples collected at representative locations and surface degassing measurements. The aim is to verify the observed anomaly pattern of alteration gradients and distinct active units, and to investigate the relationship between the optical and thermal anomaly pattern and modern degassing and hydrothermal alteration processes. In this way we provide ground truthing and demonstrate that the anomalies observed are significant.

4.2.1 Present-day surface degassing pattern

The measurements of diffuse degassing from the surface allow us to compare the present-day surface degassing pattern to the observed optical and thermal anomalies (Figure 6 A/B). We performed surface degassing measurements of CO_2, H_2S, and SO_2 simultaneously in the diffuse degassing regime at 200 measurement points (~100 points within and outside the ALTZ) throughout the whole northern crater section (details of gas measurements in Appendix B).

https://doi.org/10.5194/egusphere-2023-1692
Preprint. Discussion started: 28 July 2023

The observed relative flux values for CO_2 range from 0 to ~9000 ppmv/s with an average of ~900 ppmv/s. They are considerably higher (x*10³) than the SO_2 and H_2S flux at the respective locations. For both, SO_2 and H_2S a maximum gas flux of <10 ppmv/s was measured and the average is below 0.5 ppmv/s.

Looking at the spatial distribution of the measured gas we observed generally higher gas levels within the alteration zone ALTZ and at the ALTZ boundary, for each of the measured gas (Figure 6 C/D). The average CO_2 flux is 660 ppmv/s outside the ALTZ and 923 ppmv/s within the ALTZ. Thus, the averaged CO_2 flux inside the ALTZ is about 1.4 times higher than outside, but is particularly high in some of the constrained units a-g. However, the CO_2 flux has a wide spatial distribution and high flux values of above 2000 ppmv/s can also be observed outside the ALTZ and at a distance to the ALTZ boundary (Figure 6 A/C).

SO_2 and H_2S in contrast appear spatially stronger confined, and significant flux values can be exclusively observed within the ALTZ (Figure 6 B/D). Values for SO_2 and H_2S inside the ALTZ exceed the outside-ALTZ values by 13 and 15 times. This higher diffuse flux, although at average low concentrations, might promote a surficial process of chemical weathering and surface bleaching, potentially causing the observed color shift from a reddish-oxidized surface toward gray and will be discussed further based on analyses of the geochemical composition of rock samples in Chapter 5.2.

Comparing the surface degassing to the observed optical and thermal anomaly pattern (Figure 6 E-G), we see that high values were observed especially in units a or b on the eastern side of the fumarole field, coincident with increased alteration (Type 1 and 2) and thermally active surface, followed by other constrained units c-g. However, the strongly bleached and apparently highly altered unit c shows, other than expected, rather small values, although its surface temperature is significantly increased with respect to other identified units. This might indicate reduced surface permeability and surface sealing processes and will be discussed in chapter 5.3.

While SO_2 or H_2S flux values for Type 1 and 2 surfaces are increased, only low fluxes were constrained for the Type 3 surface and no flux for the unaltered surface (un in Figure 6 E-G). Note that the central sections of the fumarole field were not sampled due to the close vicinity to HTF and expected high flux values. The data shown here is only representative for the diffuse degassing domain.

4.2.2 Mineralogical composition of the alteration gradients

XRD Analysis was performed along two transects A and B, and XRF analysis was performed on samples taken along three transects A-C (Figure 7), crossing postulated alteration gradients.

Transect A crosses from the unaltered surface over Type 3 into the Type 1 surface of the highly altered unit c. Transect B is oriented along the HTF on the crater rim in an east-west orientation from Type 1 surface into the LTZ (Type 3). Transect C crosses the eastern fumarole field from the unaltered surface, through the Type 1 and 2 surface in unit B, the LTZ (Type 3) on both sides of the HTF, to Type 1 and 2 surface, and eventually the unaltered material outside the ALTZ.

https://doi.org/10.5194/egusphere-2023-1692
Preprint. Discussion started: 28 July 2023

Results of all samples support local alteration gradients within the ALTZ and show significant changes in the mineralogical and geochemical compositions (Table of XRD results in Appendix F). The dominant mineral phases observed in samples of transects A and B are sanidine, cristobalite, and elemental sulfur (Figure 7). Additionally, most samples contain amorphous material, representing glassy phases typical for volcanic sequences. For comparability, mineralogical concentrations refer to the crystalline phase, while amorphous contents are stated with respect to the total. Note, however, that bulk rock geochemistry refers to both phases and cannot analytically distinguish between amorphous and crystalline.

Considering compositional changes along transect A we observe a high proportion of sanidine feldspar and lesser cristobalite in the relatively unaltered samples (Type 4). With an increasing degree of alteration, we observe a general loss of cristobalite and sanidine while sulfur contents increase (Figure 7). Samples from the unaltered reddish Type 4 surface (A1) outside the ALTZ and Type 3 surface (A2/3) inside the ALTZ are similar in composition and show high sanidine and cristobalite contents of 86-87 % and 13-14% in the crystalline part, respectively, yet low to no sulfur contents. These samples were taken in areas of no or only slightly increased surface temperatures of <22°C (i.e. <5°C above the background). Samples A4-6 are taken in unit c, a complex of high alteration and increased mean surface temperatures of 28°C (~10°C above background). In this strongly altered unit, cristobalite is absent, along with a decrease in sanidine to 60-70 % relative to the least altered samples and an increase in sulfur contents of up to 20-40 % in the crystalline portion of the rock sample. However, the amorphous components constitute a high proportion of these sample(s), showing ca. 50 % in samples A6 and B1.

Samples taken on the upper rim along transect B in the high-temperature fumarole regime (V-AHT) contain total sulfur contents of 50 to 100%, while cristobalite is absent in these samples. Sample B3, a piece of grayish crust is taken from LTZ3 (~21°C, 4°C above background) in between the high-temperature fumaroles F0 and F5 and contains 100% sulfur, highlighting the precipitation and sealing potential of degassing activity at the surface.

Comparing the changes of surface coloration with changes in the mineralogical composition we can constrain no significant effect at the ALTZ boundary, i.e., the transition from unaltered to altered surface (A1-A2/3), although the optical effect is major. However, significant compositional changes, e.g. the complete loss of cristobalite and increasing sulfur content are observed at the ALT - AMT boundary (blue mark in Fig. 6), coincident with the shift from Type 3 to Type 1 surface into unit c.

4.2.3 Bulk geochemical composition of the alteration gradients

For samples without amorphous fraction, bulk geochemical composition correlates reasonably well with mineralogy determined by XRD, assuming ideal stoichiometry. The difference between theoretical bulk composition and true composition is within 10% of the respective element, which we consider a good estimate given sample heterogeneity. Only for sample A5, the high Mn content remains unmatched by XRD analysis. Subtracting the theoretical bulk composition of the crystalline fraction from the true bulk composition, we can thus estimate the chemical composition of the amorphous fraction. The amorphous fraction is similar to the crystalline counterpart mainly composed of SiO_2 and some minor (<5 wt

https://doi.org/10.5194/egusphere-2023-1692
Preprint. Discussion started: 28 July 2023

%) phases, as well as elevated Mn contents. The high Mn contents were only observed in samples with medium alteration and elevated temperatures, both in samples with and without a significant contribution portion of amorphous material. It is thus likely that Mn is contained in the crystalline phase, yet could not be detected due to the high SiO2 signals derived from sanidine and amorphous material.

The bulk geochemical composition (Figure 7 and data table in Appendix G) agrees with the mineralogical composition. All samples are high in SiO2 content and, therefore, can be considered to belong to the large silic-alteration complex earlier described by Fulignati et al. (1999). The samples show a slight variability of SiO2 between 67-82 wt. % and plot on the rhyolite field within the TAS diagram (Middlemost, 1994; not shown here). The amorphous component, typical for rhyolite, consists of mainly SiO2, with minor amounts of Fe and Al, based on the difference between the theoretical and actual geochemical composition calculated from stoichiometric mineralogy. Three samples also have significant MnO, possibly caused by hydrothermal leaching and precipitation as amorphous crusts. However, the variability of MnO will not be detailed further in this study.

Dominant in transect A is the loss of Al_2O_3 from the unaltered Type 4 surface (>10 wt.%) outside ALTZ to the Type 1 surface of the highly altered unit c (<0.4 wt.%). Similarly, Fe_2O_3 is decreasing from an average of 1.6 to 0.3 wt.%. The loss of Al_2O_3, and Fe_2O_3 is likely related to the alteration of sanidine and the elution of iron- and aluminum-sulfates formed due to the contact with sulfuric gas. The most significant changes occur, similar as observed in the mineralogy, not at the transition from unaltered to altered (ALTZ-boundary) but at the ALT-AMT boundary (blue line in figure 7) at the transition from Type 3 to Type 1 surface.

Transect C crosses from the unaltered surface through unit a, the northern LTZ, the southern LTZ, unit b, Type 3 surface, and eventually the unaltered surface. Compositional changes from unaltered (Type 4) to altered (Type 1 and 2) surface of units a and b, here, are minor with relatively stable values for Al_2O_3 (6-12%), Fe_2O_3 (1-3%), TiO_2 (<0.5) and Mn (~0). At the transition from active units a and b (Type 1 and 2 surface) to the LTZ (Type 3), we observe a significant increase of sulfur content from <2% to 12-40%. However, this increasing sulfur content here is not coincident with the systematically brighter surface color observed for other altered units. LTZ show the same rather dark surface observed for Type 3 surface elsewhere, which is a discrepancy to the effects observed in the western fumarole field and indicates that LTZ have to be considered subject to different surficial processes. This will be discussed in chapter 5.3.

5 Discussion

In this study, combining close-range remote sensing, image analysis, mineralogical and geochemical analyses of rock samples, and the investigation of the present-day surface degassing, we investigate the degassing and alteration structures of

https://doi.org/10.5194/egusphere-2023-1692
Preprint. Discussion started: 28 July 2023

the fumarole field and the broader field of activity at La Fossa cone on Vulcano. Based on image analysis (similar to Müller et al., 2021) of new better quality drone-derived high-resolution image data, we resolve the general pattern of degassing and alteration effects at the surface, spatially constrain them and complement our previous work with more detail and extensive ground truthing. In our previous work parts of the central fumarole field could not be analyzed in detail due to stronger gas plume distortion in our image data. Also, some parts of the results presented here are results of additional and intense fieldwork and lead to an adapted interpretation of observed effects especially considering the diffuse activity pattern in the eastern fumarole field.

From UAS-derived RGB imagery, we identified a ~70,000 m² sized zone that is outlining the maximum extent of observable alteration effects. We showed variability within the ALTZ that represents local alteration gradients or structural units. We show that effects of diffuse degassing and alteration can be traced far beyond the activity of high-temperature fumaroles. Alteration effects can be observed in an area (ALTZ) that is actually ~50 times larger, and a thermally active surface that is ~25 times larger than the area covered by high-temperature fumarole complexes.

Analyses of mineralogical and bulk-geochemical compositions of representative rock samples support our observations of local strong alteration gradients and allow to constrain relations between remotely sensed surface coloration and degassing and alteration processes. A general shift from reddish to gray surface coloration allows us to infer areas of increased diffuse gas flow. Variability in surface brightness and gray hues allows for the detection of alteration gradients and major active units. A largely coincident optical and thermal anomaly pattern highlights the relation between surface temperature and surface color and allows to constrain major structural units. Some of these units represent large complexes of diffuse activity and are apparently important structural features for the degassing system as will be discussed in chapter 5.3.

The presented combination of methods provides an efficient tool for first-site investigation of volcanic degassing and alteration systems and can be applied to volcanoes elsewhere. Structural findings and implications for the degassing and alteration system provide information for further and more detailed alteration research.

5.1 ALTZ controlled by sulfuric gasses and elution processes

The ALTZ, characterized by a surface color shift from reddish to gray, is coincident with the area of higher SO_2/H_2S flux and apparently represents the zone of diffuse acid gas flow (Figure 4). All measurements with a significant flow of sulfuric gas species were measured inside the ALTZ, while the flux of CO_2 was also high outside the ALTZ.

We therefore suggest the general color shift from reddish to gray to be related to this higher flux of sulfuric gasses, promoting a process of surficial chemical leaching of iron oxides, via the reduction of the initially contained iron oxides to iron sulfates, which are easily soluble in rain or condensing water vapor and prone to rapid elution. Iron oxide content in our analyzed samples ranges from 1.5% (A1) in the unaltered regime, to 1.1-1.4% for A2/3 samples to 0.3 for samples of the highly altered unit c (A4-6). There is a gradual reduction following the postulated alteration gradient, with the strongest

https://doi.org/10.5194/egusphere-2023-1692
Preprint. Discussion started: 28 July 2023

changes occurring on the ALT-AMT boundary (blue line in Figure 7). The 1.5% Fe_2O_3 for our rock sample of the unaltered regime is a rather low value and might be related to the fact that the sample was taken very close to the ALTZ boundary and consists of >50% amorphous material. Fulignati et al. (1999), who provide a broader sampling database estimated Fe_2O_3 contents of unaltered 1988-1990-eruptive products with 2.46-6.65%, which reduces to an average value below 1% in the silic-alteration regime (Fulignati et al., 1998, Fulignati et al., 1999, Boyce et al., 2007).

Evidence for chemical leaching can also be found on the crater floor, where deposits form a colored layer resembling the color spectra widely observed on La Fossa, with bright reddish deposits close to the fumarole field resembling classic fluvial patterns. We believe that the optically anomalous gray surface at Vulcano can generally be used to infer areas of present higher gas flux or former discharge of acid gasses at even low flux rates. Analyzing the broader area of the central crater region we can infer multiple other areas where we observe similar (Müller et al., 2021).

5.2 Alteration gradients on local scales

With average high SiO2 contents of >70%, the sampled areas correspond to the large silicic alteration complex suggested by Fulignati et al. (1999), Azzarini et al. (2001), Boyce et al. (2007), and others. In our study, we show evidence for strong local alteration gradients and structurally important units, spatially constrain them, and complement detail to earlier studies.

Color shifts observed within the ALTZ (brightness effects, hues of gray) are likely controlled by the degree of hydrothermal alteration, secondary mineral formation, and especially sulfur content in the respective surface samples. Coincident with characteristic changes in the surface coloration from Type 4 towards stronger bleached surfaces of Type 1, we observe a relative decrease of the initial mineral and element composition by simultaneously increasing sulfur content (Figure 7) for most of the obtained samples. While sulfur content in Type 1 surface ranges from 6 to 31 %, for Type 2 it is already below 2%, and for the unaltered fraction below 0.2%. We can, therefore, confirm a general link between alteration gradients/sulfur contents and surface brightness or surface Types in our remote sensing data (Figure 8).

An exception from this systematic are sulfur contents of the Type 3 surface. Here we observe two distinct clusters, one with values below 0.5% and one with extraordinarily high sulfur contents of 12 to >60%, both showing a similar surface coloration. All Type 3 samples with high sulfur contents are exclusively taken from LTZ. This strong discrepancy of sulfur content and surface coloration within the low-temperature zones suggests next to alteration gradients also surficial or shallow processes of mineral deposition and formation of sulfur-rich encrustations that form sealed surfaces, especially in the near field of fumaroles. The low temperatures observed within LTZ and the limited surface degassing highlight the efficiency of such sealing processes. So far we can not distinguish LTZ from Type 3 surfaces in our optical data (Figure 8). A distinction, however, would be beneficial as it would provide a method allowing for the precise spatial constraint of sealed surfaces from simple UAS-derived RGB imagery.

https://doi.org/10.5194/egusphere-2023-1692
Preprint. Discussion started: 28 July 2023

The intensity of optical and thermal effects and associated changes in mineralogical or chemical composition or degassing are not always equally significant. Although the general shift from unaltered surface to altered surface (ALTZ-boundary, shift reddish to gray) is a major criterion for the identification of degassing and alteration extent in our data, the associated changes in compositions are minor (Figure 9). The larger changes are observed within the ALTZ at the ALT-AMT boundary. Here we observe a sudden decrease in the initial mineral and bulk geochemical composition and equally increasing sulfur content. We interpret the rather low changes at the transition from unaltered to altered at the ALTZ boundary to be related to rather weak or surficial alteration effects. The size of obtained samples was on the order of ~2000 cm² including the surficial part but also material up to 10 cm depth. This way it was not possible to trace mineralogical or geochemical changes at the surface only. The samples obtained at the ALT-AMT boundary, on the other hand, show strong changes and reveal the general systematics of alteration effects, especially those samples taken in unit c, which might be considered one of the strongest alteration end members of the central crater region.

5.3 Heat budget - evidence for diffuse activity and surface sealing

Based on the gained information we outlined the surface structure of the degassing and alteration system of Vulcano (simplified in Figure 10 and detailed views of the different alteration and thermal units in Appendix C) and constrained major diffuse active units besides the HTF. To quantify their importance for the degassing and alteration system, we weigh them based on a comparison of their thermal energy release (Figure 10) for both, the contribution of anomalies with T>22°C, and identified units based on a spatial constraint, also including values >22°C.

High-temperature fumaroles of the upper fumarole field have high average radiant exitance values of 82 W/m² but can only account for 28 % of the total emitted thermal energy (calculations based on pixels with T>22°C and a corrected background of T=16.71°C). The rest of the thermal energy is released by the diffuse features described above.

Next to the HTF, multiple larger anomaly units have apparent structural importance for the degassing system. This becomes evident when analyzing the different units for their thermal energy release (Figure 10).

The second important unit is unit c. It has the second-highest average radiant exitance of 76 W/m² but exceeds the cumulative radiant flux of HTF with a contribution to the total thermal radiation of 29 %. Although it is a highly altered complex with a strongly bleached surface and increased surface temperatures there is a discrepancy to the current degassing activity. Relative gas flux values measured within unit c are lower than observed for units a and b, for instance. This might be a consequence of the dynamics of hydrothermal alteration and indicate permeability reduction or sealing processes due to the advanced state of alteration like proposed by Heap et al., 2019. This would be supported by a strong variability in mineralogical and bulk geochemical composition and associated remineralization or mineral precipitation observed in unit c.

https://doi.org/10.5194/egusphere-2023-1692
Preprint. Discussion started: 28 July 2023

Diffuse aureoles (unit a/b) on the eastern side of the fumarole cover several thousand m² each, more than the area covered by HTF, and contribute with 6 to 7 %, or about 25 % of the energy emitted by the HTF each, to the total thermal energy release. Additionally, the bleached surface, increased surface temperatures (Figure 4), and higher gas flow values (Figure 6 E-G) highlight their importance for the surficial gas-drainage capability.

Unit d and e are large diffuse features of the western fumarole field of which d is a part of the thermal aureole surrounding F0 and e a ~200m long branched anomaly, located rim parallel west of F0. Both have a similar contribution to the total thermal energy release than a and b. Unit d is separated from by F0 by a low-temperature zone (LTZ3). The transition from LTZ 3 to unit d is sudden and accompanied by a temperature jump of ~20°C. The difference in the average temperature between unit d and LTZ3 is on the order of 5 °C. Also here we observe apparent surface sealing for the whole central fumarole field. Unit f, the northern section of the F0 aureole, and anomalies in the area north of the fumarole field (g) have a minor contribution.

LTZ1-3 separating diffuse aureoles from the HTF have a Type 3 surface coloration, significantly lower temperatures, and radiant flux and exitance values than the neighboring aureole regions, which indicates processes of surface sealing. Indeed, no gas flux could not be constrained for the LTZ of the eastern fumarole field. From field observations and lab analyses (Figure 7), we constrained the LTZ as strong, sulfur-rich surface complexes which are apparently effectively sealing the surface and inhibiting gas flow. The depth of these sealed complexes can not be constrained by our data, but we can roughly constrain the spatial extent. Considering only the 3 LTZ of the central and eastern fumarole field they together cover at least an area of ~12000m², which is a significant fraction of the ALTZ. In other words, ~ 20 % of the surface of the ALTZ is apparently sealed and forces lateral gas flow to the aureole regions. This was proven by observations during the 2021 volcanic crisis at La Fossa. While at fumarole sites and diffuse active units like units a and b showed increasing mean temperatures and thermal energy release, the radiation within LTZ remained stable and low highlighting the efficiency of sealing processes. This was observed for all central LTZ and is exemplarily demonstrated by a cross-section through the eastern fumarole field section (Figure 11D).

6 Conclusion

Our investigation of the fumarole field of La Fossa cone allowed us to constrain the degassing and alteration structure, define major units of activity and quantify their importance for the degassing system, highlighting in particular large diffuse degassing areas and localized surface sealing. Our experience from the study of the degassing and alteration system at Vulcano demonstrates that close-range remote sensing studies can greatly contribute to the understanding of structural architecture or intrinsic complexities of fumarole fields. Such studies will prove beneficial for pre-site reconnaissance surveys, the detection of sampling locations for alteration-related studies and sampling grid design, and, importantly, for regular routine monitoring of hazardous volcanic crater areas and associated risk assessment.

https://doi.org/10.5194/egusphere-2023-1692
Preprint. Discussion started: 28 July 2023

7 Tables

Table 1: Overview of the processed data sets that were used for the following analyses. From The optical data, an orthomosaic and DEM were generated covering 3.74 km² with pixel resolutions of 8.6 x8.6 to 17.3 x 17.3 cm. From the high altitude infrared overflight, an infrared mosaic was acquired covering 3.23 km² with 41.2 x 41.2 cm resolution. All data sets cover the complete central section of the La Fossa cone.

Data set	Acquisition date	Pixel resolution in cm	Coverage in km²	Point density in p/m²
2019 orthomosaic	14.11..2019	8.6 x 8.6	3.74	135.20
2019 DEM	14.11.2019	17.3 x 17.3	3.74	33.41
2018 IR mosaic	15.11.2018	41.2x 41.2	3.23	5.64

8 Figures

https://doi.org/10.5194/egusphere-2023-1692
Preprint. Discussion started: 28 July 2023

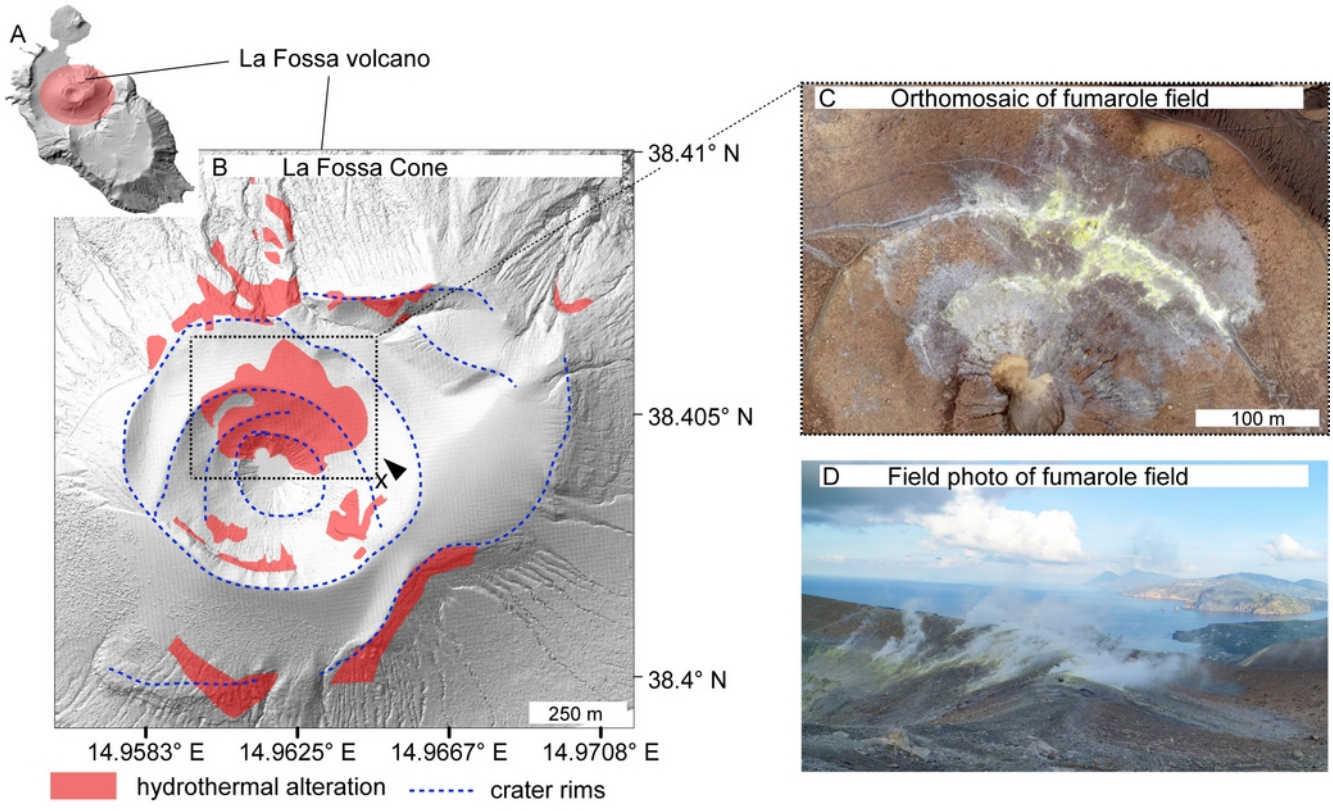

Figure 1: Overview of the degassing sites at La Fossa cone, Vulcano Island (Italy). A) Vulcano Island as shaded relief map. The red circle indicates the location of the La Fossa cone. B) Central summit region of the La Fossa Cone. Blue dashed lines depict crater rimes of different eruptive episodes. Areas of degassing and hydrothermal alteration are highlighted by red patches after Müller et al. (2021). The dashed box outlines the most prominent center of degassing and alteration, the high-temperature fumarole field. C) The high-temperature fumarole field from a birds-eye view. D) Field photograph over the fumarole field. Location and viewing direction are indicated by an x and arrow (B).

https://doi.org/10.5194/egusphere-2023-1692
Preprint. Discussion started: 28 July 2023

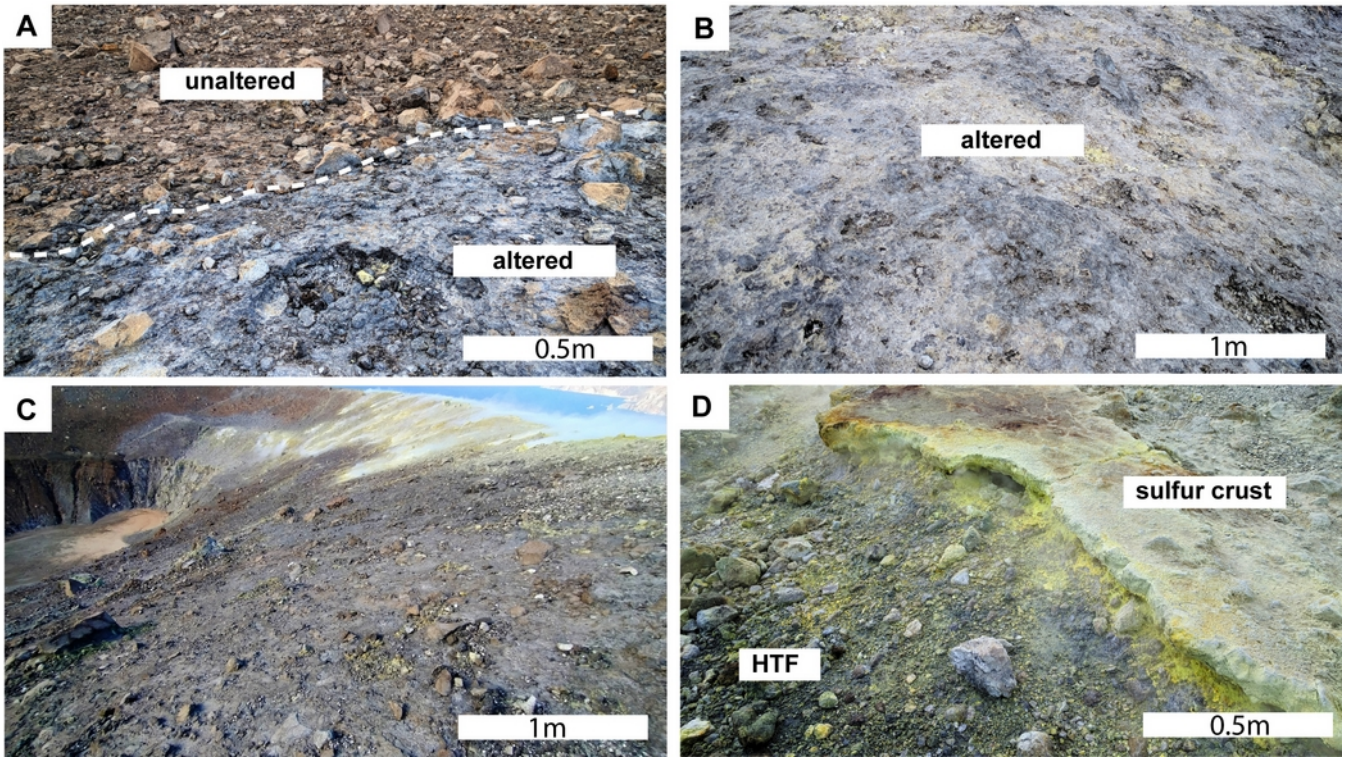

Figure 2. Different surface types and colorations in the La Fossa cone. A) Transition from unaltered to altered bleached surface. B) Intensely altered and bleached surface. C) View from the east onto sealed surfaces D) High-temperature fumarole and deposited sulfur crust.

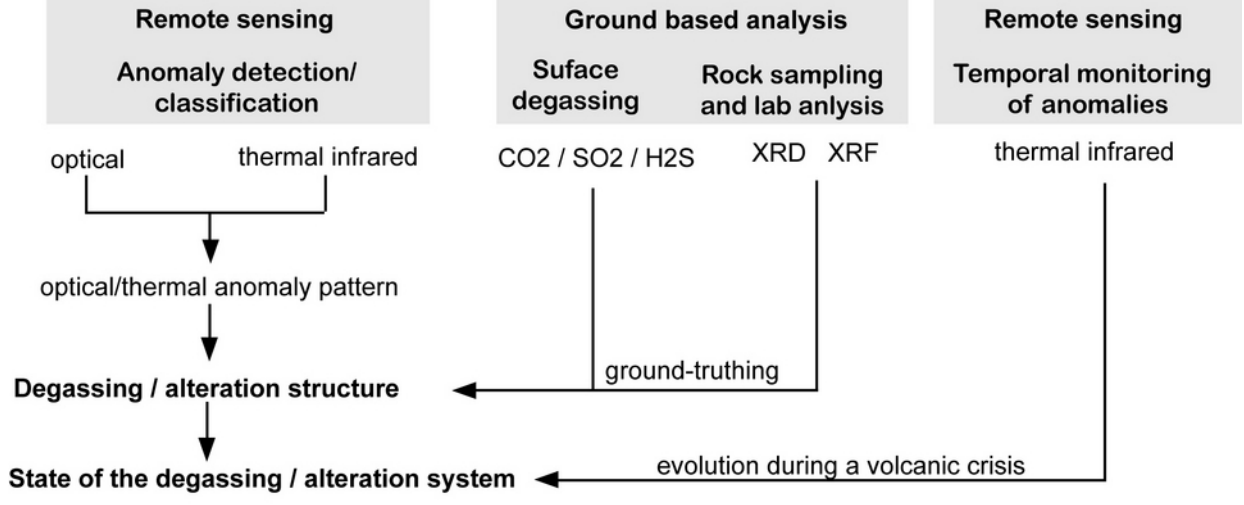

https://doi.org/10.5194/egusphere-2023-1692
Preprint. Discussion started: 28 July 2023

Figure 3: General workflow from anomaly detection from remote sensing data to ground truthing by mineralogical and geochemical investigation.

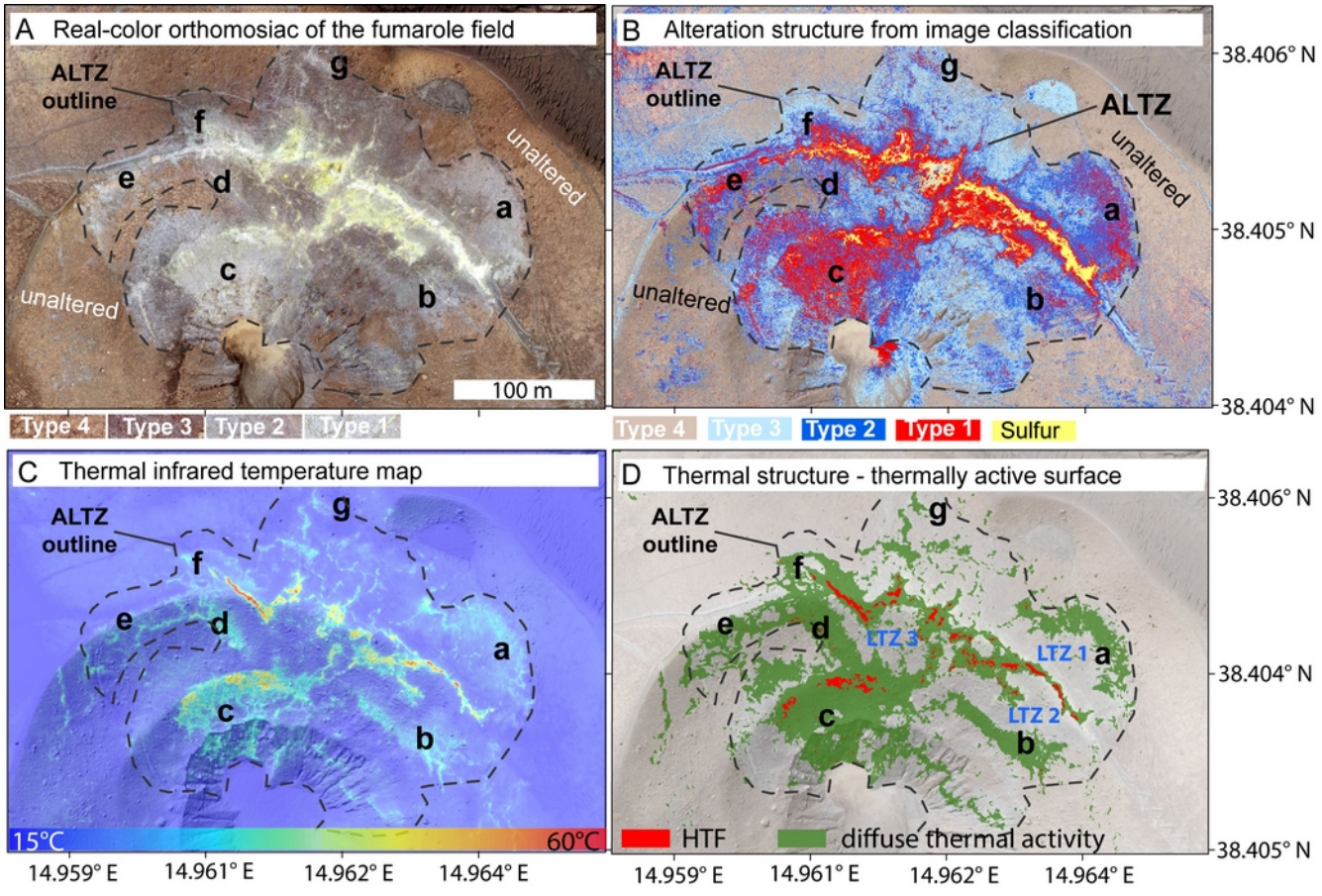

Figure 4: Alteration structure of the La Fossa fumarole field. A) True color image of the high-temperature fumarole field. B) Alteration structure of the fumarole field revealed by PCA and image classification, represented by surface Types 1-4. C) Thermal infrared image of the fumarole field. D) Simplified thermal structure of the fumarole field highlighting high-temperature fumarole location in red and diffuse thermal activity in green. Labels a-g represent notable large-scale anomaly units that can be observed in both, the alteration data and the thermal data. Note that the contrast of the background image has been reduced for highlighting in Subfigures B and D.

https://doi.org/10.5194/egusphere-2023-1692
Preprint. Discussion started: 28 July 2023

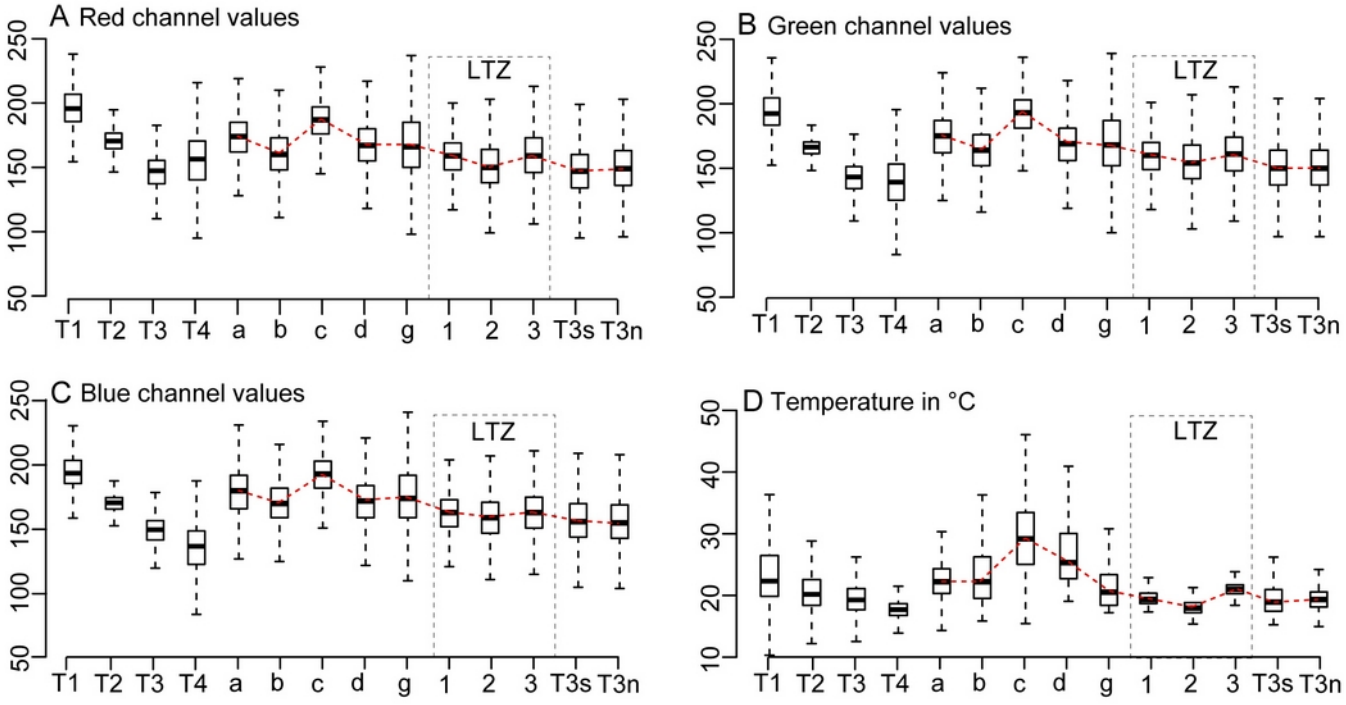

675 Figure 5: Color value- and temperature distributions for surface Types 1-4 (T1-T4), selected areas a-g, and associated low-temperature zones LTZ1-3 (location see Figure 4B/D). A) Red color value distribution. B) Green color value distribution. C) Blue color value distribution. D) Temperature value distribution. Values are based on an analysis of 6.8 million pixels within the ALTZ.

https://doi.org/10.5194/egusphere-2023-1692
Preprint. Discussion started: 28 July 2023

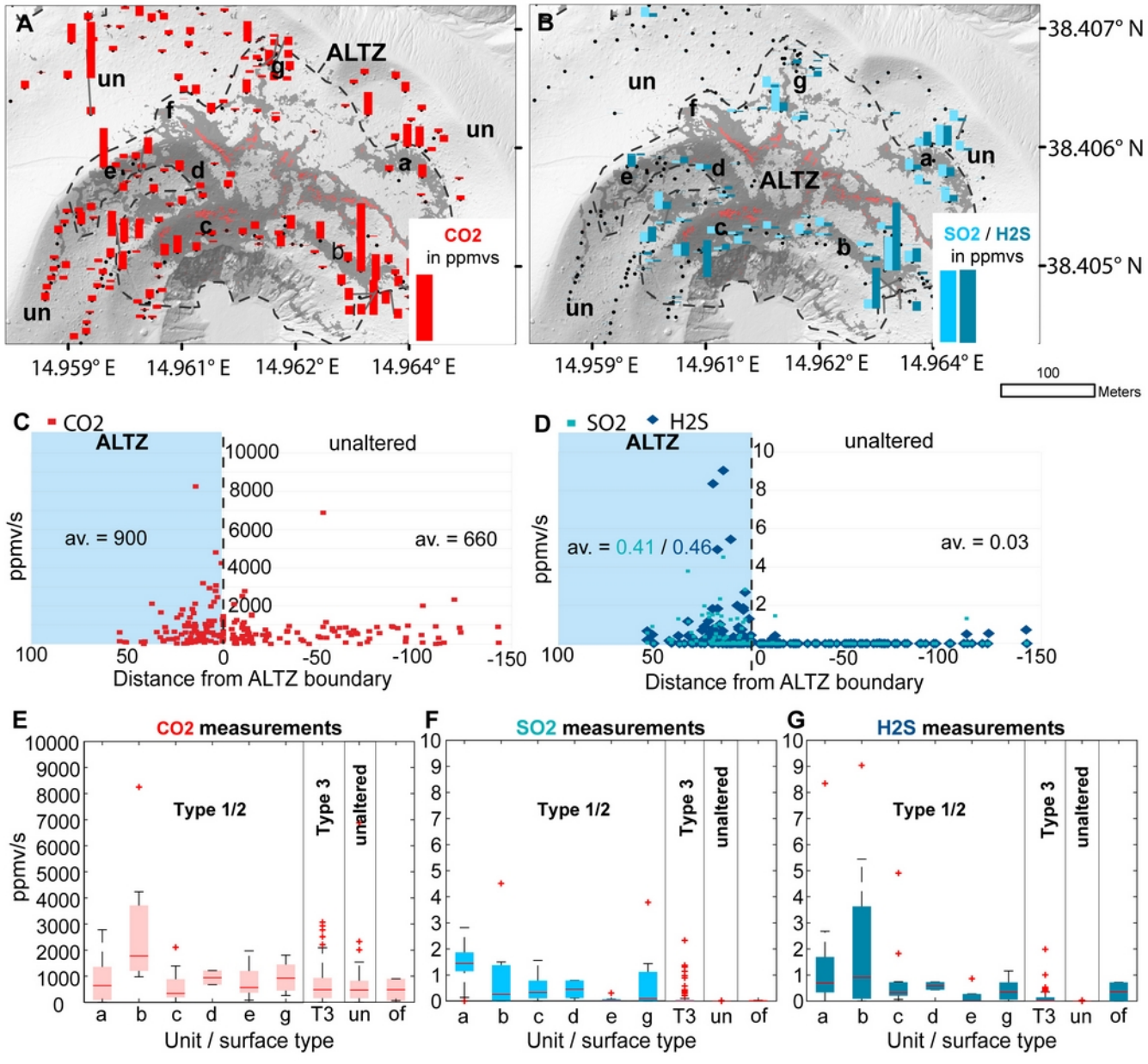

Figure 6: A/B) Spatial distribution and flux values for CO_2 (red bars in A) and SO_2/H_2S (B) in a map view. The dashed line highlights the ALTZ boundary. Dark grey features in the background highlight the thermally active surface (compare Figure 2D). C/D) Flux values within or outside the ALTZ plotted by distance to the ALTZ boundary. A generally higher flux is observed within the ALTZ, but while CO_2 (C) is also abundant outside the ALTZ, significant SO_2 and H_2S fluxes were

https://doi.org/10.5194/egusphere-2023-1692
Preprint. Discussion started: 28 July 2023

685 observed exclusively within the ALTZ, especially on the outer edges. E-G) Flux values for identified units a-g, Type 3 surface and the unaltered surface (un) highlight the lower flux of sulfuric gas species in the unaltered regime.

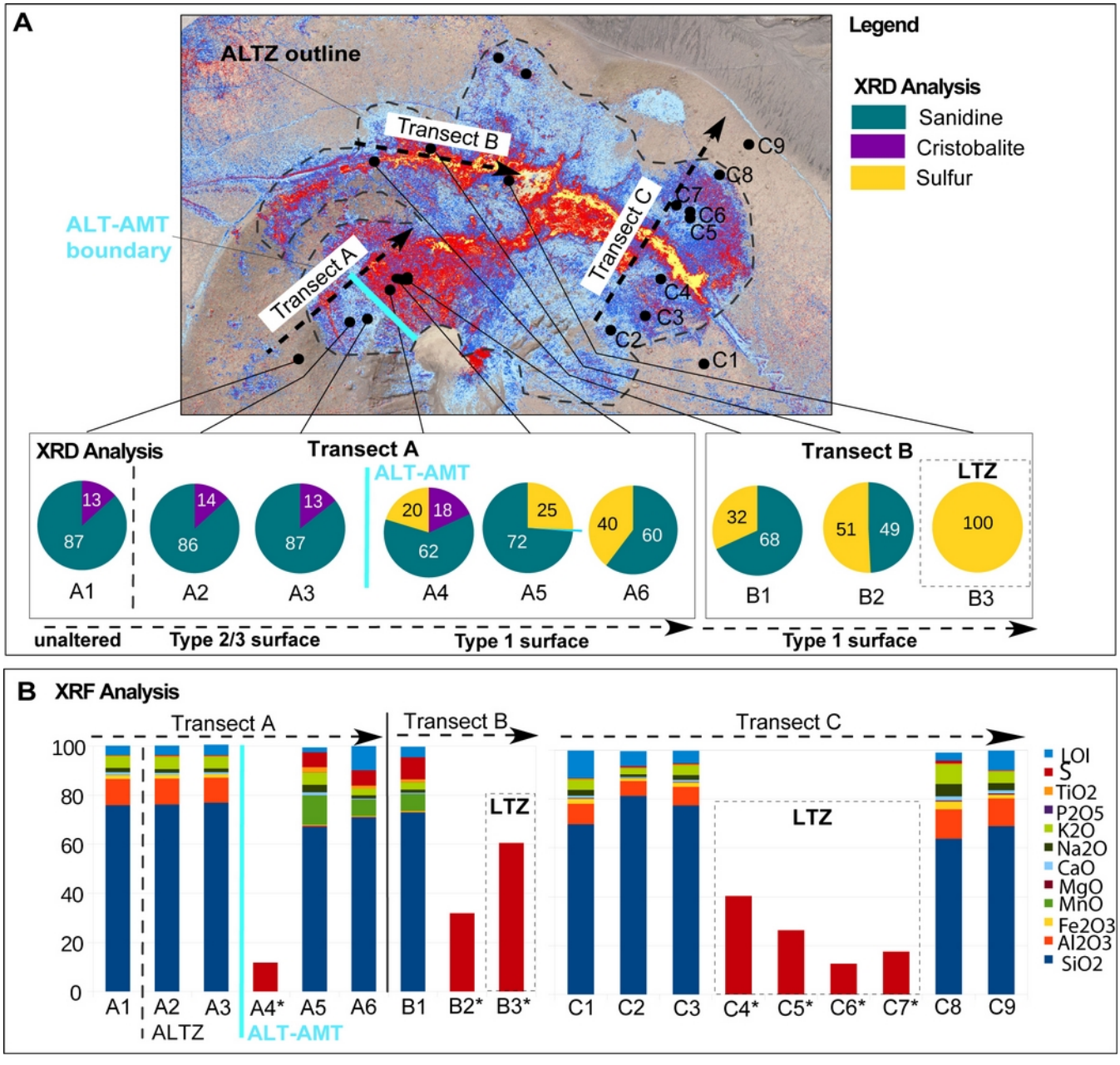

Figure 7: Mineral and chemical composition of samples along 3 transects A-C crosscutting alteration gradients and structural units. Transect A/B) With increasing alteration intensity we observe a relative decrease of the initial mineral phases sanidine

https://doi.org/10.5194/egusphere-2023-1692
Preprint. Discussion started: 28 July 2023

and cristobalite whereas the sulfur content increases. Note that the mineral composition in this figure is normalized to 100 % non-amorphous minerals. In the chemical composition, we observe a significant decrease of Al_2O_3 and Fe_2O_3 but an increase of MnO, TiO_2, and S with increasing alteration, especially at the ALT-AMT boundary. At transect C we observe a dominant increase of S 17-40% for samples taken within the LTZ. Else than observed for the other transects, changes in Al_2O_3, Fe_2O_3, TiO_2, and MnO are less significant, even in the active units a and b. For samples marked with an asterisk (*) xrf results are not available.

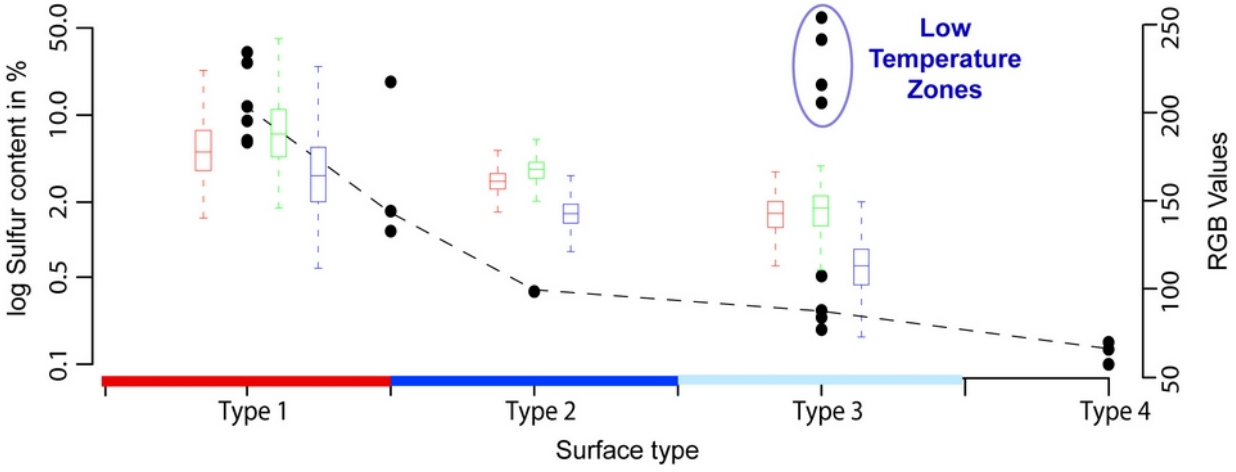

Figure 8: Overview of the relation of sulfur content of rock samples and brightness or inferred surface Type. Black dots mark the sulfur contents of rock samples, and the color-coded box plots the respective value range in the RGB values. With decreasing surface Type from highest altered (Type 1) to unaltered (Type 4), the measured sulfur contents decrease. An exemption is Type 3 surfaces where we observe two distinct clusters, one with low S-values and one with extraordinarily high S-values.

https://doi.org/10.5194/egusphere-2023-1692
Preprint. Discussion started: 28 July 2023

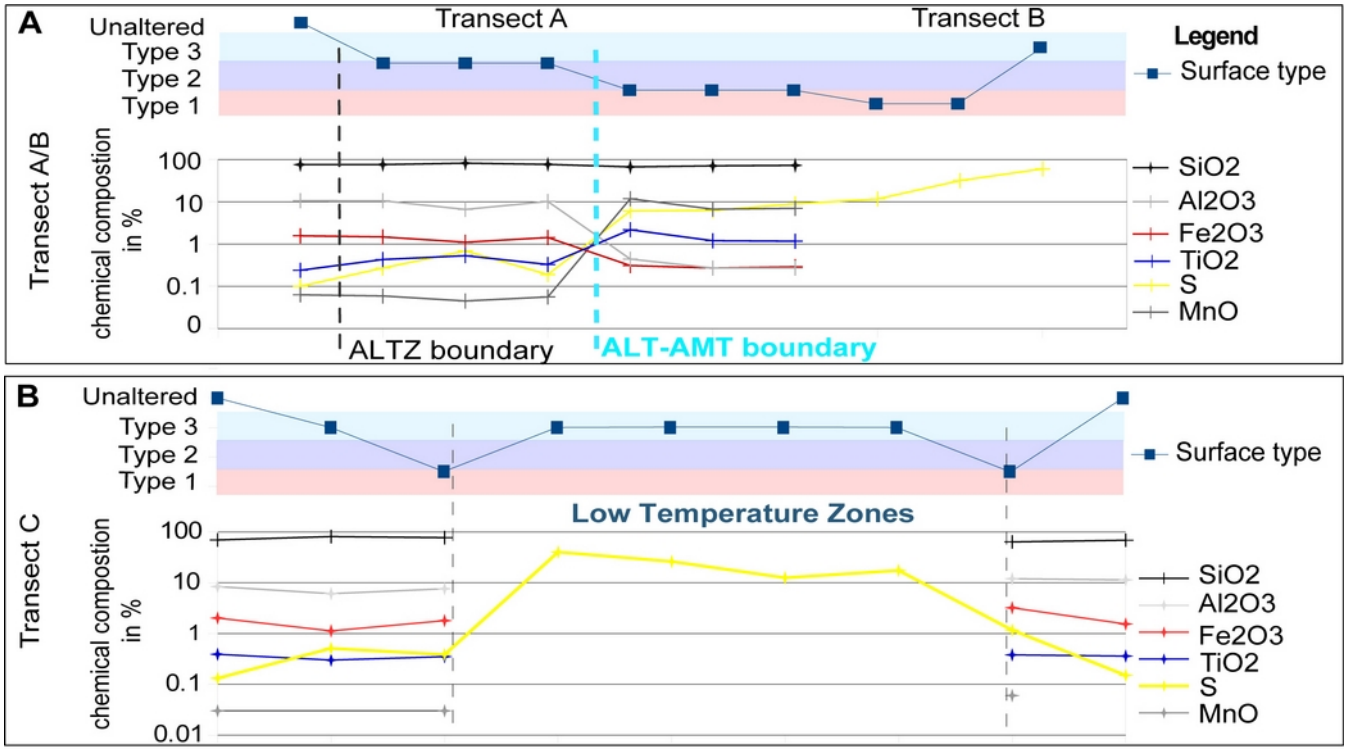

Figure 9: Geochemical changes observed along transect A-C. A) With increasing alteration from Type 4 to Type 1 surface we observe a reduction of Fe_2O_3 and Al_2O_3 and increase in S. Strongest changes are observed at the ALT-AMT boundary. B) Changes observed in the eastern fumarole field are less significant, with exception of extraordinary high sulfur content for Type 3 samples, which represent the LTZ.

https://doi.org/10.5194/egusphere-2023-1692
Preprint. Discussion started: 28 July 2023

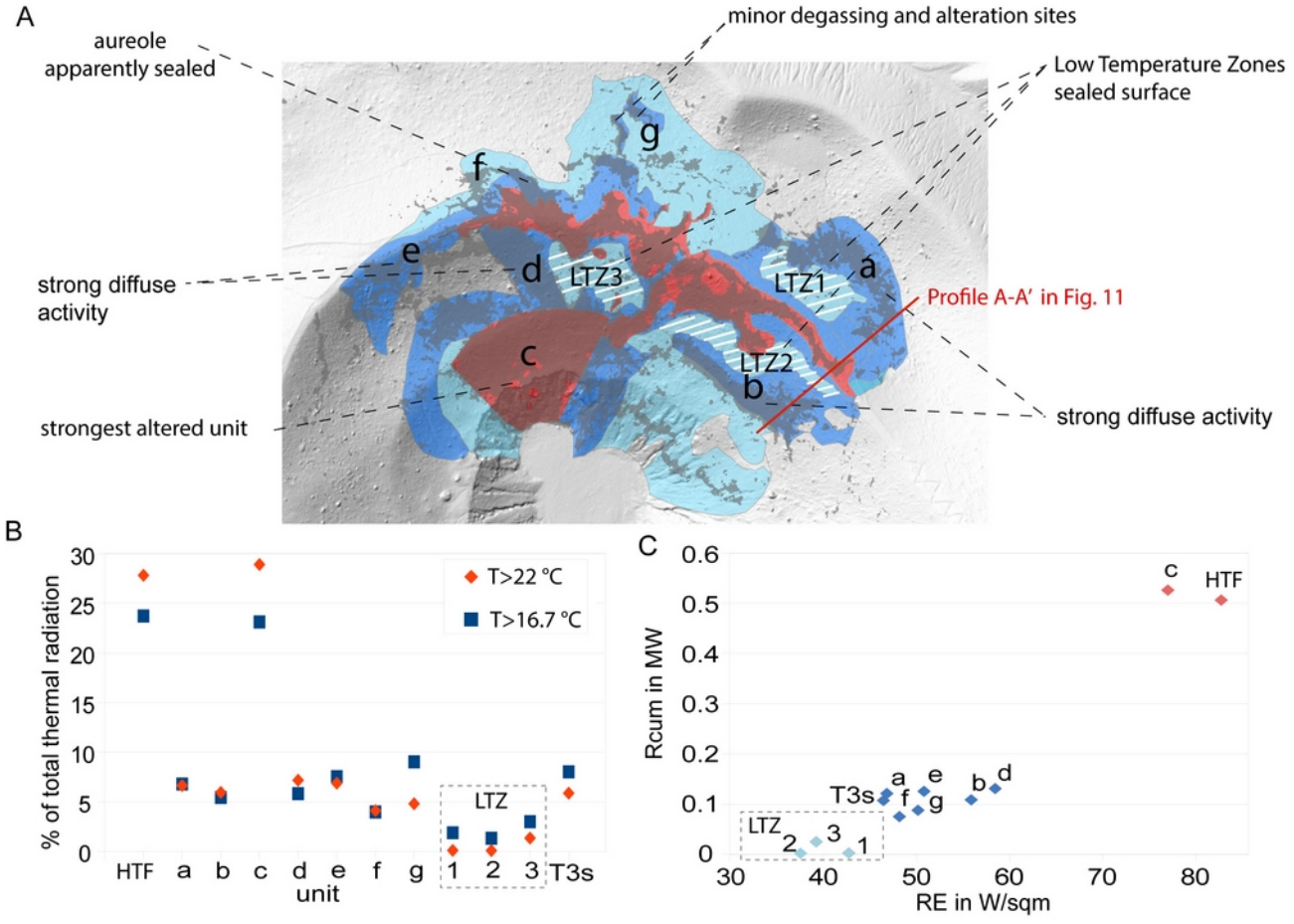

Figure 10: Anatomy of the fumarole field. A) Simplified structure of the fumarole field highlighting surface types and structural units of increased diffuse activity or apparent surface sealing (LTZ marked by white lines). B) Contribution in % to the total radiation for anomalies with T>22°C and for identified units based on a spatial constraint, also including temperatures <22 °C. C) Radiant exitance (RE) in W/m² and cumulative radiation (Rcum) in MW. Note that for RC and contribution to the total thermal radiation only anomalies with T>22°C were used.

https://doi.org/10.5194/egusphere-2023-1692
Preprint. Discussion started: 28 July 2023

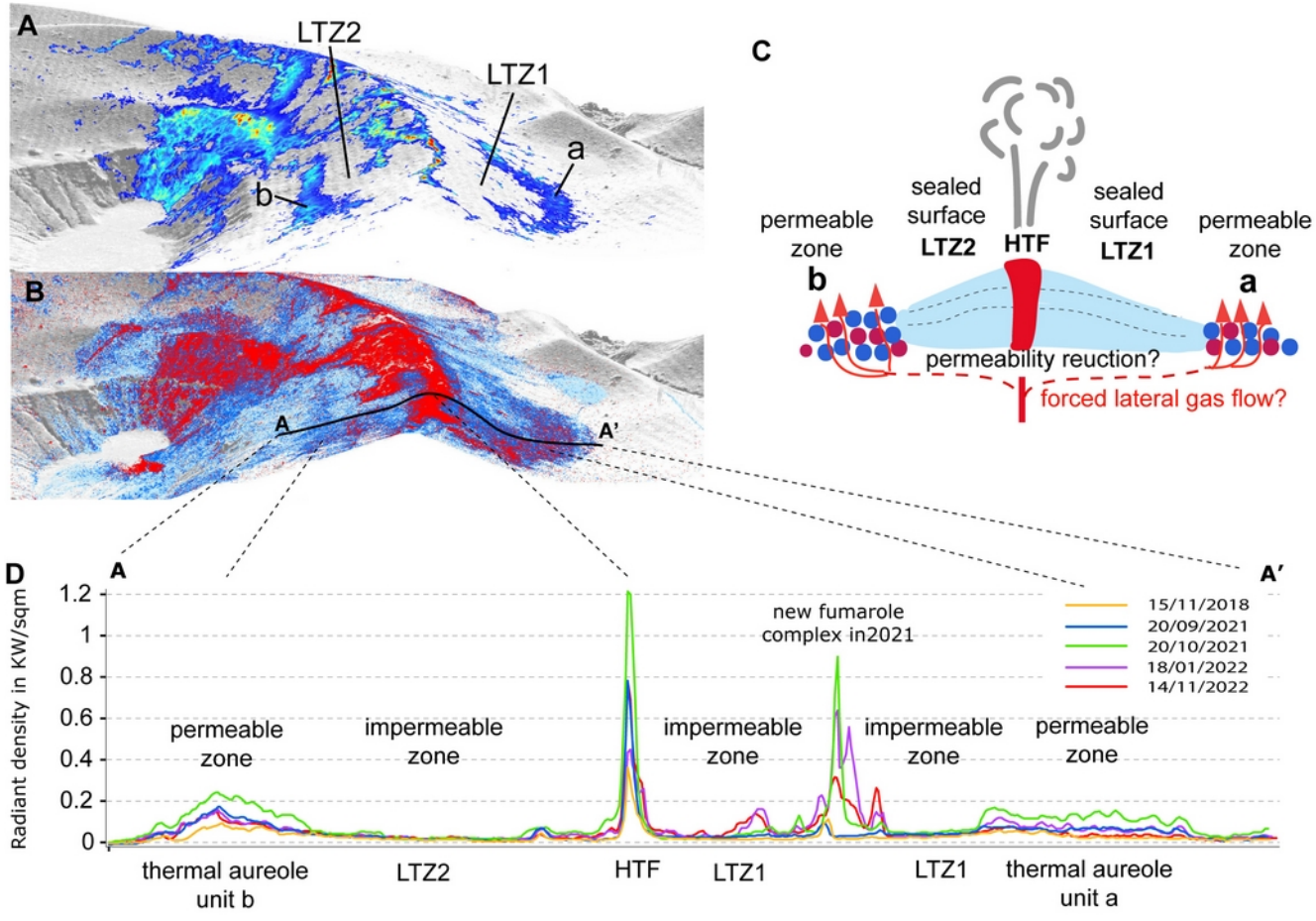

Figure 11: Crossection of the eastern fumarole field along Profile A-A' (Fig.10) highlighting the structural setup from high-temperature fumaroles in the center to LTZ and diffuse aureoles at a distance. A) Thermal structure along the cross-section. B) Alteration structure along the cross-section. C) Schematic sketch along cross-section A-A', highlighting the central LTZ that might be controlled by surface sealing processes or deeper effects of permeability reduction in the vicinity to the high-temperature fumaroles due to long-term gas-rock interaction and alteration processes. D) Evolution of thermal radiation values during a volcanic crisis. While thermal radiation at fumaroles and aureoles increased, radiation values of LTZ remain unchanged, therefore highlighting the efficiency of surface sealing.

https://doi.org/10.5194/egusphere-2023-1692
Preprint. Discussion started: 28 July 2023

9 Appendices:

Appendix A: RGB value distribution of defined surface types 1-3 within the ALTZ

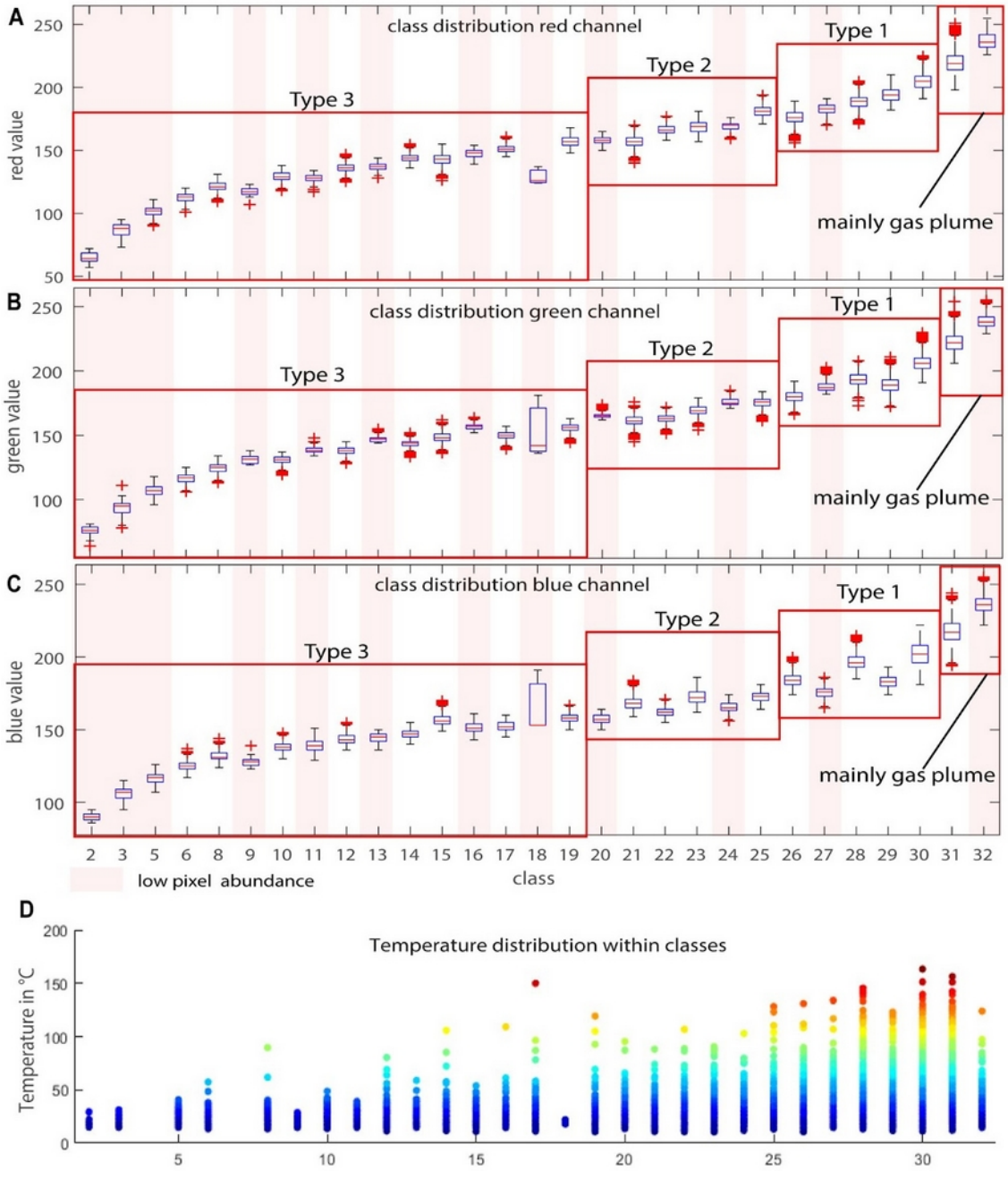

Figure A1: Boxplots of RGB value distribution for the defined surface Types 1-3. Classes (unsupervised classification 32

https://doi.org/10.5194/egusphere-2023-1692
Preprint. Discussion started: 28 July 2023

classes) marked with the transparent red bar only have minor pixel abundances. Red boxes depict the spectral range of Type 1-3 surfaces. Class 31 and 32 are mainly associated with the fumarole steam plume.

Appendix B: Gas measurement procedure - simplified accumulation chamber approach

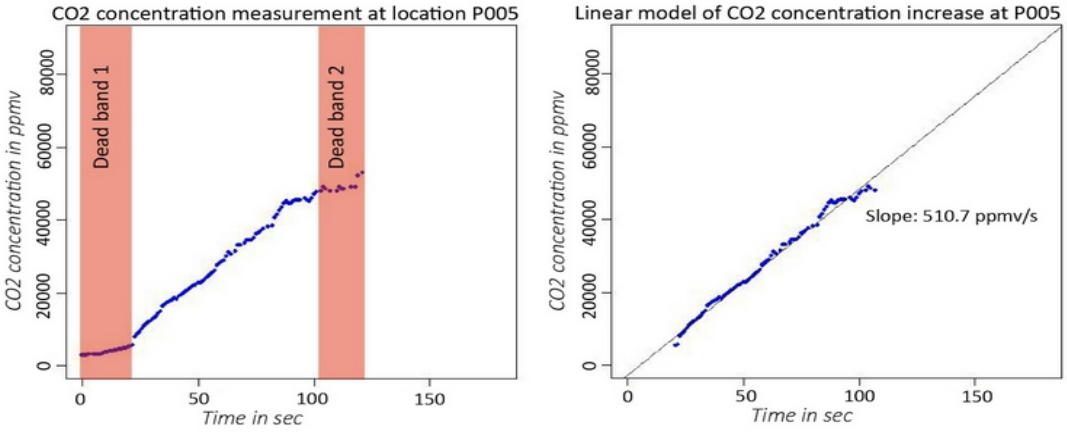

Figure B1: CO_2 measurement at location P005, here shown representative for all measurement points. Dead bands at the beginning and end of the measurement were removed and the intensity of gas flux was characterized by linear regression through the constantly ascending part of the graph. The slopes of the linear model allow a relative comparison of single measurement points.

To compare the observations from remote sensing to present-day surface degassing, measurement campaigns were performed in September 2021 and November 2022. The surface degassing was measured at 200 points within the northern part of the la fossa cone (Figure 6 in the main manuscript), in a simplified multi-gas accumulation chamber approach.

The simplified accumulation chamber consists of the measurement unit, a Dräger Xam 8000, coupled to a 10.3 cm diameter and 16.5 cm long plastic chamber by a 116 cm long tube with an inner diameter of 0.5 cm, resembling a simplified accumulation chamber. The plastic chamber has a volume of 1374.8 cm^3, the tube has a volume of 91.1 cm^3, so that the total system volume is 1465.934 cm^3. The pumping rate is 0.35l per minute. The plastic chamber was equipped with an open valve which was a necessity as the Dräger is an actively pumping system. Therefore, concentration increases in the chamber can be considered as surface flow and as independent from pumping effects. The Measurement unit is protected by a preceding 2µm filter, preventing dust and vapor to enter the unit. Note that we use Flux values in this study only for relative comparison and detection of the spatial variability of certain gas species and flows. A precise flux estimate is beyond scope of this publication and can not be constrained as we did not measure gas temperatures and humidity at sampling locations.

The measurement unit, a Dräger XAM 8000 handheld Multigas device was equipped with 6 sensors measuring CO_2, CH_4, SO_2, H_2S, H_2, and O_2 simultaneously. The relevant species for this work are CO_2, SO_2, and H_2S, therefore only these will be considered in detail. The CO_2 sensor is a Non-Dispersive Infrared (NDIR) sensor. NDIR sensors use the absorption

https://doi.org/10.5194/egusphere-2023-1692
Preprint. Discussion started: 28 July 2023

characteristics of CO_2 at ~ 4 µm, which leads to a concentration-dependent amplitude loss of the internally emitted IR light. The sensor has a detection threshold of 0.01 vol% CO_2 and is calibrated for measuring CO_2 in a range of 0-5 vol % at a resolution of 50 ppm under normal (-20-50 °C, 10-95 % RH, and 700-1300 hPa) atmospheric conditions. The response rate is < 10 sec for reaching T50- and < 15 sec for reaching T90 concentrations. The H_2S sensor is an electrochemical sensor with a detection limit of 0.4 ppm and a resolution of 0.1 ppm, measuring in a range of 0-100 ppm H_2S under normal atmospheric conditions. The response time for T90 values is >15 seconds and the accuracy of the measurement is +-5% of the measured value. The SO_2 sensor is an electrochemical sensor with a detection limit of 0.1 ppm and a resolution of 0.1 ppm, measuring as well in a range of 0-100 ppm under atmospheric conditions. The response time for T90 values is <15 seconds and the accuracy of the measurement is 2% of the measured value. The NDIR CO_2 sensor is robust against cross-sensitivities. However, electrochemical sensors can be vulnerable to cross sensitivities (SO_2, H_2S, Cl_2), resulting in uncertainties of the measurement of a few percent of the measurement value.

The approach of combining the Dräger multigas with an accumulation chamber was developed and adapted as a consequence of uncertainties encountered in previous campaigns. The different sensors have slightly different reaction times for ascending gas concentrations and significantly different reaction times for descending gas concentrations. Comparing sensor readings directly therefore might lead to odd gas ratios. For that reason instead of the direct gas readings, we use the slope of the ascending gas concentration within the accumulation chamber to produce more reliable estimates of the surface flow.

For a relative comparison of degassing rates of the single measurement points, the gas data was plotted and the representative part of the graph, resembling a constantly ascending slope, was used to calculate the concentration increase by linear regression. Data points of the “Dead Bands” at the beginning and end of each graph were removed. In this way, we achieve a relative gas flux from soil that allows us to analyze spatial variations of gas flux throughout the study area. An overview of all gas measurement points will be given in Figure 6. The aim of the gas measurements was not to provide accurate flux estimates but to highlight and quantify the spatial variability of the surface flux of certain gas species.

Each measurement was performed under similar conditions. Locations were selected in a way that they represent similar surface conditions, considering a spatial distance to fumarolic vents and an unsealed surface, for instance. Measurement locations typically were small areas with a naturally “open surface”, often embedded in broader areas of the sealed surface. Such spots typically can be identified by loose gravel on the surface and in case slightly different coloration. For the measurement, the surface was cleaned and gravel was removed to provide a flat contact surface. Then the measurement was started, and the plastic chamber was placed on the ground and sealed on the bottom with fine-grained material. The average measurement duration was 2 min. In case of very rapidly ascending SO_2 or H_2S gas concentrations, the chamber was removed from the ground before and the system was flooded with fresh air, to protect the sensors from critically high acid concentrations. This procedure was chosen to ensure a fresh air flooded chamber at the beginning of each measurement and to record the initial atmospheric gas concentration. Further, it allows better identification of the measurement start- and end-points within the respective data sets, as each data series has two dead bands, one at the beginning and one at the end. Figure B1 shows a typical graph of a CO_2 measurement, with the Dead-Band at the beginning and end of each measurement and the constant ascending graph, representing the gas concentration increase within the chamber. The “Dead Bands” represent parts of the measurement where the accumulation chamber was placed on the ground but not sealed yet, or removed from the soil at the end of the measurements. Dead Bands at the beginning of the measurement were typically on the order of 20- 30 s.

https://doi.org/10.5194/egusphere-2023-1692
Preprint. Discussion started: 28 July 2023

Appendix C: Detail views on identified units

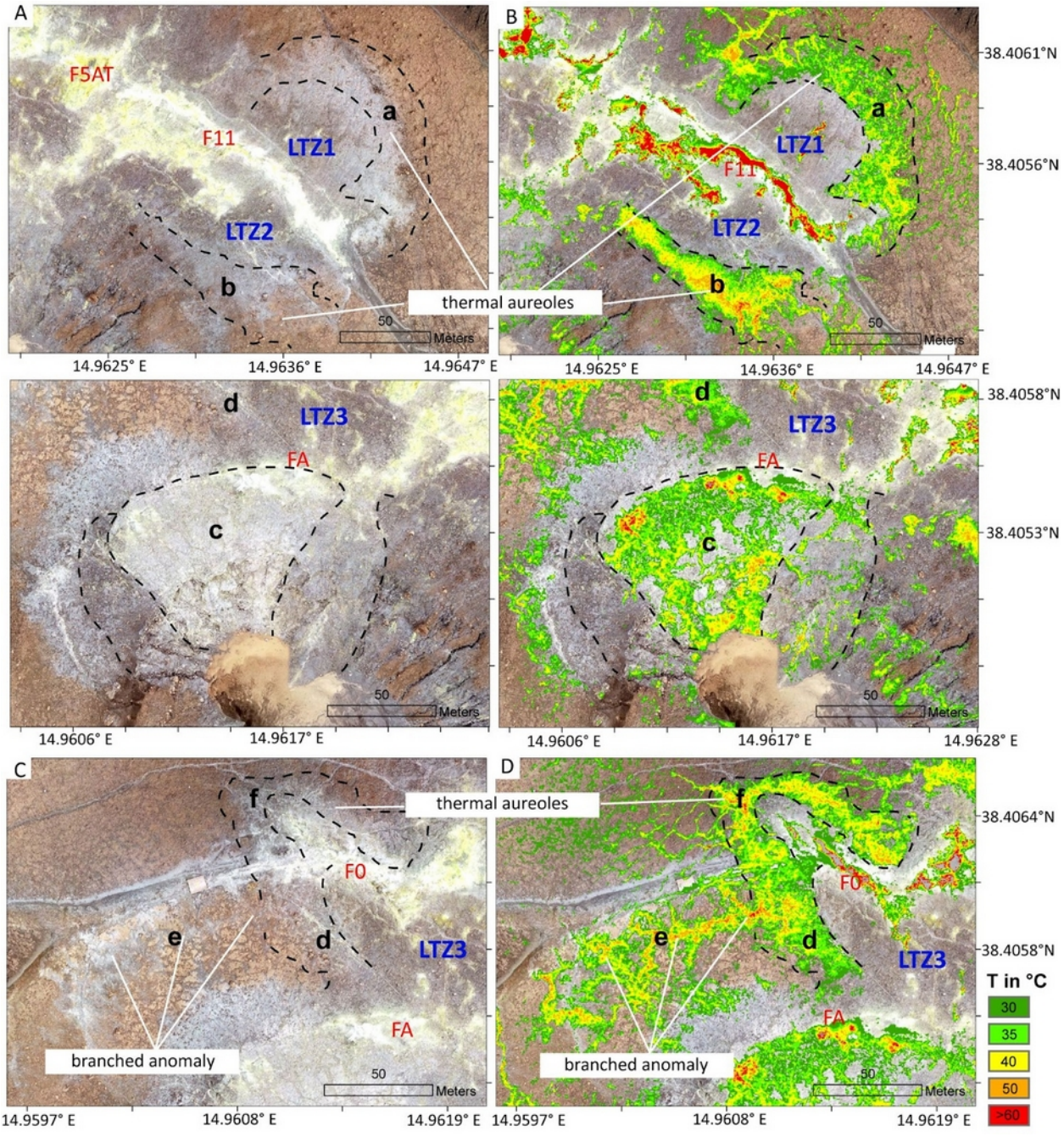

Figure C1: Detail views of distinct units a-f and LTZ1-3 in a true color representation as seen from our 2019 orthomosaic data and an overlay by the thermal data with T>30°C. A/B) Shown are units 1 and b and respective LTZ1 and 2. Note the outward spatial offset of both thermal units with respect to the surface coloration. C/D) Unit c is characterized by a network

https://doi.org/10.5194/egusphere-2023-1692
Preprint. Discussion started: 28 July 2023

of thermal anomalies embedded in colder surrounding. E/F) Thermal aureole d and f branched anomaly e. Also here an outward shift of the thermal feature with respect to the surface coloration os observed, that could indicate gradual sealing processes with proximity to the main vents.

Appendix D: Spearman correlation test for non-normal distributed variables

The test for correlation between optical and thermal anomalies was performed using the ggpubr package (Kassambara, 2019) in the statistical software environment R. The method used was Spearman's rank correlation which is suggested to be used for non-normal distributed data. The correlation test is based on the vectorized classification raster data set (classp_fumclip) with 8,890,830 data points with the analyzed variables pixel class (0-32) and pixel temperature (20- 150°C). The results show a correlation factor of 0.3485299, which is considered a mean positive correlation, and a p-value of 2.2e-16 proves statistical significance.

Spearman's rank correlation rho
data: x and y
S = 7.6277e+19, p-value < 2.2e-16
alternative hypothesis: true rho is not equal to 0
sample estimates:
rho
0.3485299

Appendix E: Thermal aureoles and LTZ indicated in field photographs

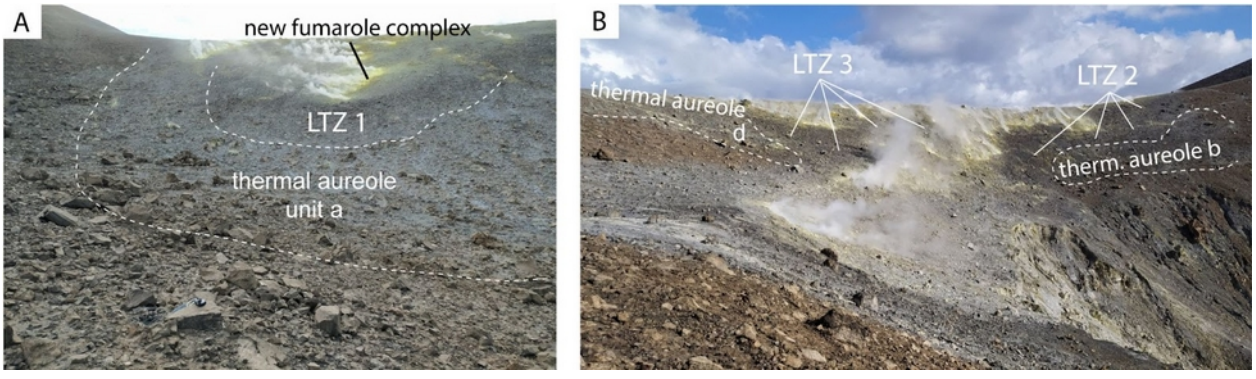

Figure E1: Thermal aureoles and low-temperature zones depicted on field photographs. A) Thermal aureole a and LTZ1. B) Thermal aureole b and d with LTZ2 and LTZ3.

https://doi.org/10.5194/egusphere-2023-1692
Preprint. Discussion started: 28 July 2023

Appendix F:

Table F1: XRD results of samples taken along transect A and B

Sample ID	A1	A2	A3	A4	A5	A6	B1	B2	B3
Sanidine	86.7	85.7	87.4	61.5	72.2	60.3	68.2	49.2	0
Cristobalite	13.3	14.3	12.6	18.2	0	0	0	0	0
Coesite	0	0	0	0	0.7	0	0	0	0
Sulfur	0	0	0	20.3	25.1	39.7	31.8	50.8	100
amorphous	50	0	0	0	0	50	50	0	0

845

Appendix G: XRF results of samples taken along transects A-C.

Table G1: XRF results of samples taken along transects A-C. Note that samples with s>10% were not analyzed by XRF.

S-ID	SiO2 (%)	TiO2 (%)	Al2O3 (%)	Fe2O3 (%)	MnO (%)	MgO (%)	CaO (%)	Na2O (%)	K2O (%)	P2O5 (%)	LOI (%)	S Eltra (%)
A1	76.0	0.2	10.7	1.6	0.1	0.1	1.1	1.8	4.8	0.1	3.8	0.1
A2	76.2	0.4	10.6	1.5	0.1	0	0.8	1.5	5.0	0.1	3.9	0.3
A3	77.0	0.3	10.2	1.4	0.1	0	0.7	1.6	4.8	0.1	4.3	0.2
A4	x	x	x	x	x	x	x	x	x	x	x	11.7
A5	67.3	2.2	0.4	0.3	11.9	0.1	1.2	3.1	5.0	0.1	2.0	6.0
A6	71.0	1.2	0.3	0.3	6.7	0.0	0.4	1.3	2.7	0.0	9.8	6.3
B1	73.0	1.2	0.3	0.3	7.0	0.0	0.5	1.3	3.0	0.0	4.3	9.0
B2	x	x	x	x	x	x	x	x	x	x	x	31.9
B3	x	x	x	x	x	x	x	x	x	x	x	60.5
C1	69.7	0.4	8.4	2.0	0	0.3	1.0	2.4	4.2	0.1	11.3	0.1
C2	81.3	0.3	6.1	1.1	0	0.1	0.4	1.1	2.5	0	6.1	0.5

https://doi.org/10.5194/egusphere-2023-1692
Preprint. Discussion started: 28 July 2023

C3	77.4	0.4	7.6	1.8	0	0.2	0.9	2.0	4.0	0.1	5.1	0.4
C4	x	x	x	x	x	x	x	x	x	x	x	40.3
C5	x	x	x	x	x	x	x	x	x	x	x	26.2
C6	x	x	x	x	x	x	x	x	x	x	x	12.5
C7	x	x	x	x	x	x	x	x	x	x	x	17.5
C8	63.8	0.4	12.0	3.2	0.1	0.4	1.7	5.0	8.0	0.1	3.2	1.2
C9	68.9	0.4	11.4	1.5	0	0.4	1.3	3.0	4.7	0.1	8.1	0.2

10 Data availabilty

Data will be made available on request for now and will be published on Zenodo in case of acceptance for revision during revision of this manuscript.

11 Author contributions

D.M conceptualized the study, collected data, performed the remote sensing and gas analysis, and led the manuscript writing. T.R.W. provided funding, supported the conceptualization, and supervised the writing. V.T. supported the conceptualization, performed XRD analysis, and supervised the writing. J.S. performed XRF analysis and supported the writing. A.K. performed XRD analysis and supported the writing. E.D.P. collected data and samples, supported all field works and the writing of this manuscript. A.F.P. supported fieldwork and on the ground logistics, acquired data, and supported the writing. M.Z. supported the gas measurement campaign and supported the writing. B.D.J. supported the fieldwork and writing of this manuscript.

12 Competing interests

The authors declare that they have no conflict of interest.

https://doi.org/10.5194/egusphere-2023-1692
Preprint. Discussion started: 28 July 2023

13 Acknowledgements

We are grateful for the financial and material support provided to realize this study. This work is contributing to the focus cite Etna and was financially supported by GFZ Potsdam. Financial support to realize this study was also provided by DAAD research grant Nr. 57556282. We thank INGV Palermo for collaboration and their support especially during the 2021 crisis, without parts of this study could not have been realized. Further we want to acknowledge the Swedish Research Council.

14 References

Aiuppa, A., Federico, C., Giudice, G., & Gurrieri, S. (2005). Chemical mapping of a fumarolic field: La Fossa crater, Vulcano Island (Aeolian Islands, Italy). *Geophysical Research Letters*, *32*(13). https://doi.org/10.1029/2005GL023207

Azzarini, F. M., Pareschi, M. T., Sbrana, A., Favalli, M., & Fulignati, P. (2001). Surface hydrothermal alteration mapping at Vulcano Island using MIVIS data. *International Journal of Remote Sensing*, *22*(11), 2045-2070. https://doi.org/10.1080/01431160118291

Ball, M. and Pinkerton, H., 2006. Factors affecting the accuracy of thermal imaging cameras in volcanology. *Journal of Geophysical Research: Solid Earth*, *111*(B11). https://doi.org/10.1029/2005JB003829

Barreca, G., Bruno, V., Cultrera, F., Mattia, M., Monaco, C., & Scarfì, L. (2014). New insights in the geodynamics of the Lipari–Vulcano area (Aeolian Archipelago, southern Italy) from geological, geodetic and seismological data. *Journal of Geodynamics*, *82*, 150-167. https://doi.org/10.1016/j.jog.2014.07.003

Berg, S. E., Troll, V. R., Harris, C., Deegan, F. M., Riishuus, M. S., Burchardt, S., & Krumbholz, M. (2018). Exceptionally high whole-rock δ18O values in intra-caldera rhyolites from Northeast Iceland. *Mineralogical Magazine*, *82*(5), 1147-1168. https://doi.org/10.1180/mgm.2018.114

BILLI, Andrea, et al. Tectonics and seismicity of the Tindari Fault System, southern Italy: Crustal deformations at the transition between ongoing contractional and extensional domains located above the edge of a subducting slab. *Tectonics*, 2006, 25. Jg., Nr. 2. https://doi.org/10.1029/2004TC001763

Bolognesi, L., & D'Amore, F. (1993). Isotopic variation of the hydrothermal system on Vulcano Island, Italy. *Geochimica et Cosmochimica Acta*, *57*(9), 2069-2082. https://doi.org/10.1016/0016-7037(93)90094-D

Boyce, A. J., Fulignati, P., Sbrana, A., & Fallick, A. E. (2007). Fluids in early stage hydrothermal alteration of high-sulfidation epithermal systems: A view from the Vulcano active hydrothermal system (Aeolian Island, Italy). *Journal of Volcanology and Geothermal Research*, *166*(2), 76-90. https://doi.org/10.1016/j.jvolgeores.2007.07.005

https://doi.org/10.5194/egusphere-2023-1692
Preprint. Discussion started: 28 July 2023

Bukumirovic, T., Italiano, F., & Nuccio, P. M. (1997). The evolution of a dynamic geological system: the support of a GIS for geochemical measurements at the fumarole field of Vulcano, Italy. *Journal of volcanology and geothermal research*, *79*(3-4), 253-263. https://doi.org/10.1016/S0377-0273(97)00032-2

Capasso, G., Favara, R., Inguaggiato, S., 1997. Chemical features and isotopic composition of gaseous manifestations on Vulcano Island, Aeolian Islands, Italy: an interpretative model of fluid circulation. Geochim. Cosmochim. Acta 61, 3425–3440 https://doi.org/10.1016/S0016-7037(97)00163-4

Capasso, G., Favara, R., & Inguaggiato, S. (2000). Interaction between fumarolic gases and thermal groundwaters at Vulcano Island (Italy): evidences from chemical composition of dissolved gases in waters. *Journal of volcanology and geothermal research*, *102*(3-4), 309-318. https://doi.org/10.1016/S0377-0273(00)00193-1

Capasso, G., Federico, C., Madonia, P., & Paonita, A. (2014). Response of the shallow aquifer of the volcano-hydrothermal system during the recent crises at Vulcano Island (Aeolian Archipelago, Italy). *Journal of volcanology and geothermal research*, *273*, 70-80. https://doi.org/10.1016/j.jvolgeores.2014.01.005

Carapezza, M. L., Barberi, F., Ranaldi, M., Ricci, T., Tarchini, L., Barrancos, J., ... & Gattuso, A. (2011). Diffuse CO2 soil degassing and CO2 and H2S concentrations in air and related hazards at Vulcano Island (Aeolian arc, Italy). *Journal of Volcanology and Geothermal Research*, *207*(3-4), 130-144. https://doi.org/10.1016/j.jvolgeores.2011.06.010

Carranza, E. J. M., & Hale, M. (2002). Mineral imaging with Landsat Thematic Mapper data for hydrothermal alteration mapping in heavily vegetated terrane. *International journal of remote sensing*, *23*(22), 4827-4852. https://doi.org/10.1080/01431160110115014

Chiodini, G., Cioni, R., & Marini, L. (1993). Reactions governing the chemistry of crater fumaroles from Vulcano Island, Italy, and implications for volcanic surveillance. *Applied Geochemistry*, *8*(4), 357-371. https://doi.org/10.1016/0883-2927(93)90004-Z

Chiodini, G., Allard, P., Caliro, S., Parello, F., 2000. 18O exchange between steam and carbon dioxide in volcanic and hydrothermal gases: Implications for the source of water. Geochim. Cosmochim. Acta 64, 2479–2488 https://doi.org/10.1016/S0016-7037(99)00445-7

Chiodini, G., Frondini, F., & Raco, B. (1996). Diffuse emission of CO 2 from the Fossa crater, Vulcano Island (Italy). *Bulletin of Volcanology*, *58*, 41-50. https://doi.org/10.1007/s004450050124

Chiodini, G., Granieri, D., Avino, R., Caliro, S., Costa, A., & Werner, C. (2005). Carbon dioxide diffuse degassing and estimation of heat release from volcanic and hydrothermal systems. *Journal of Geophysical Research: Solid Earth*, *110*(B8). https://doi.org/10.1029/2004JB003542

https://doi.org/10.5194/egusphere-2023-1692
Preprint. Discussion started: 28 July 2023

Clarke, A. B., Ongaro, T. E., & Belousov, A. (2015). Vulcanian eruptions. In *The encyclopedia of volcanoes* (pp. 505-518). Academic Press. https://doi.org/10.1016/B978-0-12-385938-9.00028-6

Coppola, D., Laiolo, M., Campus, A., & Massimetti, F. (2022). Thermal unrest of a fumarolic field tracked using VIIRS imaging bands: The case of La fossa crater (Vulcano Island, Italy). *Frontiers in Earth Science*, *10*, 964372. https://doi.org/10.3389/feart.2022.964372

Cultrera F., Barreca G., Ferranti L., Monaco C., Pepe F., Passaro S., Barberi G., Bruno V., Burrato P., Mattia M., Musumeci C., Scarfì L.; Structural architecture and active deformation pattern in the northern sector of the Aeolian-Tindari-Letojanni fault system (SE Tyrrhenian Sea-NE Sicily) from integrated analysis of field, marine geophysical, seismological and geodetic data. *Italian Journal of Geosciences* 2017;; 136 (3): 399–417. https://doi.org/10.3301/IJG.2016.17

Darmawan, H., Troll, V. R., Walter, T. R., Deegan, F. M., Geiger, H., Heap, M. J., ... & Müller, D. (2022). Hidden mechanical weaknesses within lava domes provided by buried high-porosity hydrothermal alteration zones. *Scientific Reports*, *12*(1), 3202. https://doi.org/10.1038/s41598-022-06765-9

De Astis, G., La Volpe, L., Peccerillo, A., & Civetta, L. (1997). Volcanological and petrological evolution of Vulcano island (Aeolian Arc, southern Tyrrhenian Sea). *Journal of Geophysical Research: Solid Earth*, *102*(B4), 8021-8050. https://doi.org/10.1029/96JB03735

De Astis, G., Lucchi, F., Dellino, P., La Volpe, L., Tranne, C. A., Frezzotti, M. L., & Peccerillo, A. (2013). Chapter 11 Geology, volcanic history and petrology of Vulcano (central Aeolian archipelago). *Geological Society, London, Memoirs*, *37*(1), 281-349. https://doi.org/10.1144/M37.11

Di Tommaso, I., & Rubinstein, N. (2007). Hydrothermal alteration mapping using ASTER data in the Infiernillo porphyry deposit, Argentina. *Ore Geology Reviews*, *32*(1-2), 275-290. https://doi.org/10.1016/j.oregeorev.2006.05.004

Diliberto, I. S. (2013). Time series analysis of high temperature fumaroles monitored on the island of Vulcano (Aeolian Archipelago, Italy). *Journal of volcanology and geothermal research*, *264*, 150-163. https://doi.org/10.1016/j.jvolgeores.2013.08.003

Diliberto, I. S. (2017). Long-term monitoring on a closed-conduit volcano: A 25 year long time-series of temperatures recorded at La Fossa cone (Vulcano Island, Italy), ranging from 250 C to 520 C. *Journal of Volcanology and Geothermal Research*, *346*, 151-160. https://doi.org/10.1016/j.jvolgeores.2017.03.005

Diliberto, I., Pedone, M., Jácome Paz, M., Inguaggiato, S., Mazot, A., Cangemi, M. and Pisciotta, A.F., 2021. Volcanic Gas Hazard Assessment in the Baia di Levante Area (Vulcano Island, Italy) Inferred by Geochemical Investigation of Passive Fluid Degassing. Environmental Geosciences, 11. https://doi.org/10.3390/geosciences11110478

Donoghue, E., Troll, V. R., Harris, C., O'Halloran, A., Walter, T. R., & Torrado, F. J. P. (2008). Low-temperature hydrothermal alteration of intra-caldera tuffs, Miocene Tejeda caldera, Gran Canaria, Canary Islands. *Journal of Volcanology and Geothermal Research*, *176*(4), 551-564. https://doi.org/10.1016/j.jvolgeores.2008.05.002

https://doi.org/10.5194/egusphere-2023-1692
Preprint. Discussion started: 28 July 2023

Donoghue, E., Troll, V. R., & Harris, C. (2010). Fluid–rock interaction in the Miocene, Post-Caldera, Tejeda intrusive complex, Gran Canaria (Canary Islands): insights from mineralogy, and O-and H-isotope geochemistry. *Journal of Petrology*, *51*(10), 2149-2176. https://doi.org/10.1093/petrology/egq052

Fischer, T. P., Ramírez, C., Mora-Amador, R. A., Hilton, D. R., Barnes, J. D., Sharp, Z. D., ... & Shaw, A. M. (2015). Temporal variations in fumarole gas chemistry at Poás volcano, Costa Rica. *Journal of Volcanology and Geothermal Research*, *294*, 56-70. https://doi.org/10.1016/j.jvolgeores.2015.02.002

Fulignati, P., Gioncada, A., & Sbrana, A. (1998). Geologic model of the magmatic-hydrothermal system of vulcano (Aeolian Islands, Italy). *Mineralogy and Petrology*, *62*(3-4), 195.

Fulignati, P., Gioncada, A., & Sbrana, A. (1999). Rare-earth element (REE) behaviour in the alteration facies of the active magmatic–hydrothermal system of Vulcano (Aeolian Islands, Italy). *Journal of Volcanology and geothermal research*, *88*(4), 325-342.
https://doi.org/10.1016/S0377-0273(98)00117-6

Fulignati, P. (2020). Clay minerals in hydrothermal systems. *Minerals*, *10*(10), 919.
https://doi.org/10.3390/min10100919

Gertisser, R., Troll, V. R., Walter, T. R., Nandaka, I. G. M. A., & Ratdomopurbo, A. (Eds.). (2023). *Merapi Volcano: Geology, Eruptive Activity, and Monitoring of a High-Risk Volcano*. Springer Nature. https://doi.org/10.1007/978-3-031-15040-1

Giggenbach, W.F. (1996). Chemical Composition of Volcanic Gases. In: Monitoring and Mitigation of Volcano Hazards. Springer, Berlin, Heidelberg.
https://doi.org/10.1007/978-3-642-80087-0_7

Halldórsson, S. A., Hilton, D. R., Troll, V. R., & Fischer, T. P. (2013). Resolving volatile sources along the western Sunda arc, Indonesia. *Chemical Geology*, *339*, 263-282.
https://doi.org/10.1016/j.chemgeo.2012.09.042

Harris, A. J., Lodato, L., Dehn, J., & Spampinato, L. (2009). Thermal characterization of the Vulcano fumarole field. *Bulletin of Volcanology*, *71*, 441-458.
https://doi.org/10.1007/s00445-008-0236-8

Harris, A., Alparone, S., Bonforte, A., Dehn, J., Gambino, S., Lodato, L., & Spampinato, L. (2012). Vent temperature trends at the Vulcano Fossa fumarole field: the role of permeability. *Bulletin of volcanology*, *74*, 1293-1311. https://doi.org/10.1007/s00445-012-0593-1

Heap, M.J., Troll, V.R., Kushnir, A.R.L., Gilg, H.A., Collinson, A.S.D., Deegan, F.M., Darmawan, H., Seraphine, N., Neuberg, J. and Walter, T.R., 2019. Hydrothermal alteration of andesitic lava domes can lead to explosive volcanic behaviour. Nature Communications, 10(1): 5063. https://doi.org/10.1038/s41467-019-13102-8

https://doi.org/10.5194/egusphere-2023-1692
Preprint. Discussion started: 28 July 2023

Heap, M. J., & Violay, M. E. (2021). The mechanical behaviour and failure modes of volcanic rocks: a review. *Bulletin of Volcanology*, *83*(5), 33. https://doi.org/10.1007/s00445-021-01447-2

Henley, R. W., & McNabb, A. (1978). Magmatic vapor plumes and ground-water interaction in porphyry copper emplacement. *Economic Geology*, *73*(1), 1-20. https://doi.org/10.2113/gsecongeo.73.1.1

Inguaggiato, S., Vita, F., Diliberto, I. S., Inguaggiato, C., Mazot, A., Cangemi, M., & Corrao, M. (2022). The volcanic activity changes occurred in the 2021–2022 at Vulcano island (Italy), inferred by the abrupt variations of soil CO2 output. *Scientific Reports*, *12*(1), 21166. https://doi.org/10.3390/rs14051283

Julia, F., Vladimir, L., Sergey, R., & David, Z. (2014). Effects of hydrothermal alterations on physical and mechanical properties of rocks in the Kuril–Kamchatka island arc. *Engineering Geology*, *183*, 80-95. https://doi.org/10.1016/j.enggeo.2014.10.011

Kassambara, A. (2020). ggpubr:'ggplot2'based publication ready plots. R package version 0.4. 0.

Kereszturi, G., Schaefer, L. N., Miller, C., & Mead, S. (2020). Hydrothermal alteration on composite volcanoes: mineralogy, hyperspectral imaging, and aeromagnetic study of Mt Ruapehu, New Zealand. *Geochemistry, Geophysics, Geosystems*, *21*(9), e2020GC009270. https://doi.org/10.1029/2020GC009270

Liuzzo, M., Di Muro, A., Giudice, G., Michon, L., Ferrazzini, V., & Gurrieri, S. (2015). New evidence of CO2 soil degassing anomalies on P iton de la F ournaise volcano and the link with volcano tectonic structures. *Geochemistry, Geophysics, Geosystems*, *16*(12), 4388-4404. https://doi.org/10.1002/2015GC006032

Lynch, D.K., Hudnut, K.W. and Adams, P.M., 2013. Development and growth of recently-exposed fumarole fields near Mullet Island, Imperial County, California. Geomorphology, 195: 27-44. https://doi.org/10.1016/j.geomorph.2013.04.022

Madonia, P., Cusano, P., Diliberto, I. S., & Cangemi, M. (2013). Thermal anomalies in fumaroles at Vulcano island (Italy) and their relationship with seismic activity. *Physics and Chemistry of the Earth, Parts A/B/C*, *63*, 160-169. https://doi.org/10.1016/j.pce.2013.06.001

Madonia, P., Cangemi, M., Costa, M., & Madonia, I. (2016). Mapping fumarolic fields in volcanic areas: A methodological approach based on the case study of La Fossa cone, Vulcano island (Italy). *Journal of volcanology and geothermal research*, *324*, 1-7. https://doi.org/10.1016/j.jvolgeores.2016.05.014

Mannini, S., Harris, A. J., Jessop, D. E., Chevrel, M. O., & Ramsey, M. S. (2019). Combining ground-and ASTER-based thermal Measurements to Constrain fumarole field heat budgets: The case of Vulcano Fossa 2000–2019. *Geophysical Research Letters*, *46*(21), 11868-11877. https://doi.org/10.1029/2019GL084013

https://doi.org/10.5194/egusphere-2023-1692
Preprint. Discussion started: 28 July 2023

Mia, B., & Fujimitsu, Y. (2012). Mapping hydrothermal altered mineral deposits using Landsat 7 ETM+ image in and around Kuju volcano, Kyushu, Japan. *Journal of Earth System Science*, *121*, 1049-1057. https://doi.org/10.1007/s12040-012-0211-9

Middlemost, E. A. (1994). Naming materials in the magma/igneous rock system. *Earth-science reviews*, *37*(3-4), 215-224. https://doi.org/10.1016/0012-8252(94)90029-9

Minissale, A., Donato, A., Procesi, M., Pizzino, L. and Giammanco, S., 2019. Systematic review of geochemical data from thermal springs, gas vents and fumaroles of Southern Italy for geothermal favourability mapping. Earth-Sci Rev, 188: 514-535. https://doi.org/10.1016/j.earscirev.2018.09.008

Müller, D., Bredemeyer, S., Zorn, E., De Paolo, E., & Walter, T. R. (2021). Surveying fumarole sites and hydrothermal alteration by unoccupied aircraft systems (UAS) at the La Fossa cone, Vulcano Island (Italy). *Journal of Volcanology and Geothermal Research*, *413*, 107208. https://doi.org/10.1016/j.jvolgeores.2021.107208

Nuccio, P. M., & Paonita, A. (2001). Magmatic degassing of multicomponent vapors and assessment of magma depth: application to Vulcano Island (Italy). *Earth and Planetary Science Letters*, *193*(3-4), 467-481. https://doi.org/10.1016/S0012-821X(01)00512-X

Paonita, A., Federico, C., Bonfanti, P., Capasso, G., Inguaggiato, S., Italiano, F., ... & Sortino, F. (2013). The episodic and abrupt geochemical changes at La Fossa fumaroles (Vulcano Island, Italy) and related constraints on the dynamics, structure, and compositions of the magmatic system. *Geochimica et cosmochimica acta*, *120*, 158-178. https://doi.org/10.1016/j.gca.2013.06.015

Pirajno, F. (2009). Hydrothermal Processes and Wall Rock Alteration. In: Hydrothermal Processes and Mineral Systems. Springer, Dordrecht. https://doi.org/10.1007/978-1-4020-8613-7_2

Reid, M. E., Sisson, T. W., & Brien, D. L. (2001). Volcano collapse promoted by hydrothermal alteration and edifice shape, Mount Rainier, Washington. *Geology*, *29*(9), 779-782. https://doi.org/10.1130/0091-7613(2001)029%3C0779:VCPBHA%3E2.0.CO;2

Rowan, L. C., Wetlaufer, P. H., & Stewart, J. H. (1976). Discrimination of rock Types and detection of hydrothermally altered areas in south-central Nevada by the use of computer-enhanced ERTS images.

Stevenson, J.A. and Varley, N., 2008. Fumarole monitoring with a handheld infrared camera: Volcán de Colima, Mexico, 2006–2007. *Journal of Volcanology and Geothermal Research*, *177*(4), pp.911-924. https://doi.org/10.1016/j.jvolgeores.2008.07.003

Tayebi, M.H., Tangestani, M.H. & Vincent, R.K. Sub-pixel mapping of iron-bearing minerals using ALI data and MTMF algorithm, Masahim volcano, SE Iran. *Arab J Geosci* 8, 3799–3810 (2015). https://doi.org/10.1007/s12517-014-1400-4

https://doi.org/10.5194/egusphere-2023-1692
Preprint. Discussion started: 28 July 2023

Troll, V. R., Hilton, D. R., Jolis, E. M., Chadwick, J. P., Blythe, L. S., Deegan, F. M., ... & Zimmer, M. (2012). Crustal CO2 liberation during the 2006 eruption and earthquake events at Merapi volcano, Indonesia. *Geophysical Research Letters*, *39*(11). https://doi.org/10.1029/2012GL051307

Toutain, J.-P., Sortino, F., Baubron, J.-C., Richon, P., Surono, Sumarti, S. and Nonell, A., 2009. Structure and CO2 budget of Merapi volcano during inter-eruptive periods. B Volcanol, 71(7): 815-826. https://doi.org/10.1007/s00445-009-0266-x

Van der Meer, F. D., Van der Werff, H. M., Van Ruitenbeek, F. J., Hecker, C. A., Bakker, W. H., Noomen, M. F., ... & Woldai, T. (2012). Multi-and hyperspectral geologic remote sensing: A review. *International Journal of Applied Earth Observation and Geoinformation*, *14*(1), 112-128. https://doi.org/10.1016/j.jag.2011.08.002